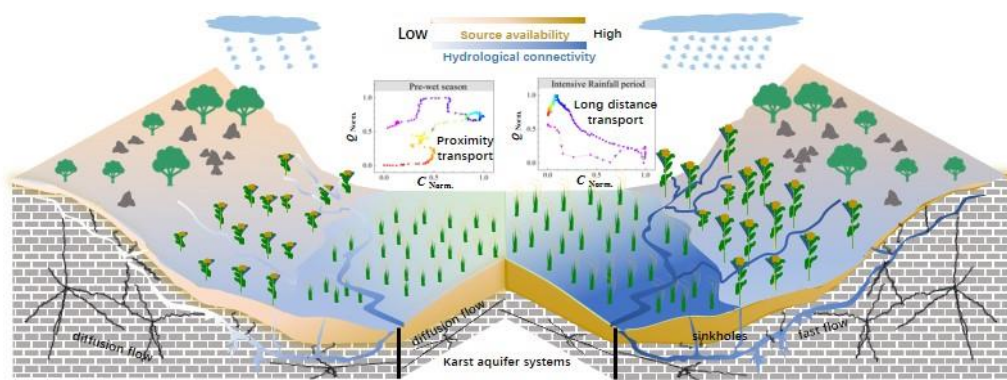


Graphic Abstract



**Source availability and hydrological connectivity determined nitrate-
discharge relationships during rainfall events in karst catchment as
revealed by high-frequency nitrate sensing**

Fu-Jun Yue ^{a,b}, Si-Liang Li ^{a*}, Susan Waldron ^b, David M. Oliver ^c, Xi Chen ^a, Pan Li ^a,
Tao Peng^d, Cong-Qiang Liu ^a

^a Institute of Surface-Earth System Science, School of Earth System Science, Tianjin
University, Tianjin 300072, China;

^b School of Geographical and Earth Sciences, University of Glasgow, Glasgow G12
8QQ, United Kingdom;

^c Biological & Environmental Sciences, Faculty of Natural Sciences, University of
Stirling, Stirling FK9 4LA, United Kingdom;

^d State Key Laboratory of Environmental Geochemistry, Institute of Geochemistry,
Chinese Academy of Sciences, Guiyang 550081, China;

**Corresponding author:* Prof. siliang.li@tju.edu.cn;

Fax, +86 (0) 22 27405051

Abstract Karst terrain seasonal monsoonal rainfall is often associated with high concentrations of nitrate-N in streams draining agricultural land. Such high concentrations can pose problems for environmental and human health. However, the relationship between rainfall events that mobilize nitrate and resulting nitrate export remains poorly understood in karst terrain. To better understand the processes that drive nitrate dynamics during rainfall events, the characteristics of individual rainfall events were analyzed using sensor technology. Thirty-eight rainfall events were separated from the high-frequency dataset spanning 19 months at a karst spring site. The results revealed that nitrate-discharge (N-Q) hysteresis in 79% of rainfall events showed anticlockwise hysteresis loop patterns, indicating nitrate export from long distances within short event periods. Karstic hydrological connectivity and source availability were considered two major determining factors of N-Q hysteresis. Gradual increase in hydrological connectivity during intensive rainfall period accelerated nitrate transportation by karst aquifer systems. Four principal components (PCs, including antecedent conditions PC1&3 and rainfall characteristics PC2&4 explained 82% of the cumulative variance contribution to the rainfall events. Multiple linear regression of four PCs explained more than 50% of the variation of nitrate loading and amplitude during rainfall events, but poorly described nitrate concentrations and hydro-chemistry parameters, which may be influenced by other factors, e.g., nitrate transformation, fertilization time and water-rock interaction. Although variation of N concentration during event flow is evident, accounting for antecedent conditions and rainfall factors can help to predict rainfall event N loading during rainfall events. Pollution of the karstic catchment occurred by a flush of nitrate input following rainfall events; antecedent and rainfall conditions are therefore important factors to consider for the water quality management. Reducing source availability during the wet season may

facilitate to reduction of nitrogen loading in similar karst areas.

Keywords: Concentration-discharge, Hysteresis, Rainfall event, Antecedent conditions, Hydrological connectivity

1 Introduction

Increasing world population and growing demands on food production have contributed to excessive application of fertilizers in many agricultural landscapes globally (Gallo et al., 2015; Gu et al., 2015). This has often led to the leaching of nitrogen (N), in a water-soluble form (nitrate, NO_3^-), into surface and ground waters (Carrey et al., 2021; Wang et al., 2020). Elevated concentrations of NO_3^- in water can pose a risk to both aquatic ecosystem health and human health (Lassaletta et al., 2014; Zhang et al., 2015), with acceptable limits in drinking water sources defined by the World Health Organisation (WHO) as $\text{NO}_3^- < 50 \text{ mg/L}$.

NO_3^- concentration ($[\text{NO}_3^- - \text{N}]$) in receiving waters and export from fields, farms and catchments is governed by land use and biogeochemical cycling (Gallo et al., 2015; Gao and Yu, 2020; Vaughan et al., 2017). Rainfall events alter water availability in catchments and can mobilize nitrate, initiating transport and delivery of increased levels of nitrate loading to receiving waters, particularly during heavy or intense storms (Li et al., 2022; Rue et al., 2017). Heavy rain can lead to the saturation of soil within a short period of time, accelerate nutrient leaching and thus promote nutrient export (Wang et al., 2020; Yang et al., 2013). Rainfall, through its timing, intensity and duration, is therefore an important factor that can influence nutrient cycling and wider catchment water quality (Lang et al., 2013; Ostrom and Davis, 2019; Wollheim et al., 2017).

As one type of fragile ecosystem, the unique karst aquifers can be conceptualized as a dual-flow system, comprised of underground channels and surface flows (Ford and

Williams, 2013). Previous studies in karst area found that dual flow systems are particularly vulnerable to anthropogenic pollution because of the direct connectivity, high transmissivity and poor self-purification (Ford et al., 2019; Green et al., 2019; Yang et al., 2020), which results in nitrate concentrations frequently exceeding the threshold of drinking water standards (Ming et al., 2020; Wang et al., 2020). The rapid hydrological response of karst aquifer systems to rainfall events poses a challenge to understanding N behavior during event flow (Huebsch et al., 2014; Opsahl et al., 2017). Recent studies have identified that hydrological and climatological factors, such as rainfall characteristics, hydrological connectivity and structure can influence nitrate behavior (Husic et al., 2020; Wang et al., 2023; Yue et al., 2020). However, the influence of these factors on nitrate behavior in karst areas remains unclear.

Previous studies have shown that the relationship between hydrological condition and N behavior can be determined using high-frequency monitoring approaches that generate long time-series datasets (e.g. > annual cycle) (Blaen et al., 2017; Opsahl et al., 2017; Rose et al., 2018). In situ and online monitoring of $[\text{NO}_3^- - \text{N}]$ has advanced through developments in high-frequency sensor technology (Duncan et al., 2017; Kraus et al., 2017). This technology can capture the fine-scale temporal patterns of nitrate dynamics and help to decrease uncertainty in estimates of nitrate loading to receiving waters relative to low-frequency sampling (Vaughan et al., 2017; Wollheim et al., 2017). These high-resolution datasets can also help to further support our understanding of the mechanisms that control nitrate responses during rainfall-runoff events, e.g., by identifying key processes responsible for nitrate behavior. Therefore, such datasets record multiple rainfall events of varying characteristics and can inform our understanding of nitrogen transport during high-loading export periods in karst landscapes.

To understand nitrate behavior during rainfall events, quantitative analysis of the relationship between nitrate concentration (N) and discharge (Q) can reveal important information on pollutant source and transfer dynamics in catchments (Butturini et al., 2008; Lawler et al., 2006). Patterns of emergence of concentration (C) with Q during the rising and falling limb of storm hydrographs vary depending on factors such as proximity and magnitude of pollutant source and this results in common typologies of hysteresis (Liu et al., 2021; Zhang et al., 2016a). For example, clockwise hysteresis occurs when the pollutant/solute concentration peak is ahead of the Q peak, which suggests that the source of the solute is in close proximity, possibly even in-stream, and transferred rapidly to the receiving water and associated monitoring site (Lloyd et al., 2016a; Vaughan et al., 2017). In contrast, anticlockwise hysteresis often reflects a pollutant source that is more distant from the point of monitoring (Bowes et al., 2015; Butturini et al., 2008). Complex hysteretic patterns, e.g., “figure-of-eight” patterns comprising clockwise and anticlockwise hysteresis indicate intra-catchment solute transport of varying size or a combination of runoff generation processes (Keesstra et al., 2019).

Coupled with a flushing index (FI), which signals the directional change in solute concentration at the onset of event flow and at peak flow during rising limb (Rose et al., 2018; Vaughan et al., 2017), these two indices can indicate timing, flushing behavior and proximity of biogeochemical sources (Keesstra et al., 2019; Lloyd et al., 2016b). In addition, multivariate statistics of high-frequency data (e.g., meteorology, concentration, discharge, and hydro-chemical parameters) provide insight into solute biogeochemistry during rainfall events. As a multivariate statistical method, principal component analysis (PCA) can identify the relationship between the original indicator variables and transform them into independent principal components (PCs) (Blaen et

al., 2017; Yang et al., 2013). Based on PCA, multiple linear regression (MLR) can use to estimate the unknown regression coefficient, which has been widely used for multiple parameters analysis during rainfall events to identify the mechanism of solute behaviors (Lawniczak et al., 2016; Mahler et al., 2008). Therefore, data collected through high-frequency sensor technology can provide improved underpinning evidence to support and develop C and Q relationship analysis further (Lloyd et al., 2016b).

The karst terrain in Southwestern (SW) China, located in the centre of one of the three largest continuous karst areas in the world, has an annual rainfall of up to 1600 mm (Green et al., 2019; Jiang et al., 2014). The monsoon climate drives a strongly seasonal rainfall distribution, with more than 70% of annual precipitation delivered during the wet season (May to October), which coincides with the plant-growing season (Jiang et al., 2014; Song et al., 2017). The wet season is therefore an important period for nitrate export due to increased nitrate loading to land from agricultural activities coupled with the elevated potential for leaching from the soil layer (Pu et al., 2011; Yue et al., 2019). To date, there are no reports of the various characteristics of nitrate behavior, e.g., N-Q response patterns, source area, loading, during differing hydrological conditions over a long-term time series, particularly during the key nitrate export periods, e.g. rainfall events. Understanding this may further benefit effective karst catchment management.

This study focused on a typical Chinese karst landscape, where the long-term and high-resolution characterization of $[\text{NO}_3^- - \text{N}]$ has previously been reported to be as high as 16.3 mg/L among five sites (Yue et al., 2019). To understand nitrate behavior during rainfall events in the karst area, one karst spring Laoheitan (LHT) with more available long-term high-frequency data of discharge and nitrate concentration than the other four

sites was selected. The characteristics of 38 individual rainfall events occurring over 19 months were used to analyze nitrate responses to discharge (N-Q). The aims of the present study were to (i) understand N-Q response patterns to rainfall events in karst area; (ii) quantify the influence of rainfall-runoff events on nitrate export; and (iii) determine what factors, e.g. antecedent conditions, rainfall characteristics, karst aquatic system, and to what extent explain the variance of nitrate export during rainfall events.

2 Materials and methods

2.1 Study Area

Karst geomorphology in SW China includes features such as well-developed sinkholes, fractures and conduit structures (Jiang et al., 2014; Liu, 2007). The monitoring site was located at LHT in the middle reaches of the Houzhai Catchment within Puding Karst Critical Zone Observatory in Puding county, Guizhou province (E 26° 13' 22.4", N105° 44' 20.4") (Figure 1). This site was established in 1978 for long-term monitoring. The LHT station drains a 17.69 km² catchment area with Maguan town and the Muzudong reservoir (MZD-Re) located in the catchment (Figure 1b).

The catchment geomorphology changes from high-density cone topography with many depressions and very thin soil in the upper reaches of the catchment, to forested hillslopes with valleys in the middle reaches. Natural vegetation, including forest, shrub and grass, accounts for 59.2% of LHT sub-catchment. Agricultural land, including dryland (21.2%) and paddy field (11.5%), is mainly distributed within the valley depressions in the upper reaches and across the plains in the middle reaches of the catchment. Crops grown are typically rice/corn-canola rotation and vegetables. The major crops in summer season are rice, corn and various vegetables, while crops in the winter season are canola and a few vegetables. Organic fertilizers such as cattle and pig manure are seasonally applied at the beginning of major crop tillage periods, typically

for rapeseed (November) and rice (May). Synthetic fertilizers, urea and diammonium phosphate are also applied to land during the growing season (May to July for summer crops and November for winter crops). The total fertilization amounts to 198.4 - 224.9 kg/ha, and N fertilizer contributes 74.5% of fertilizer use (Liang et al., 2020).

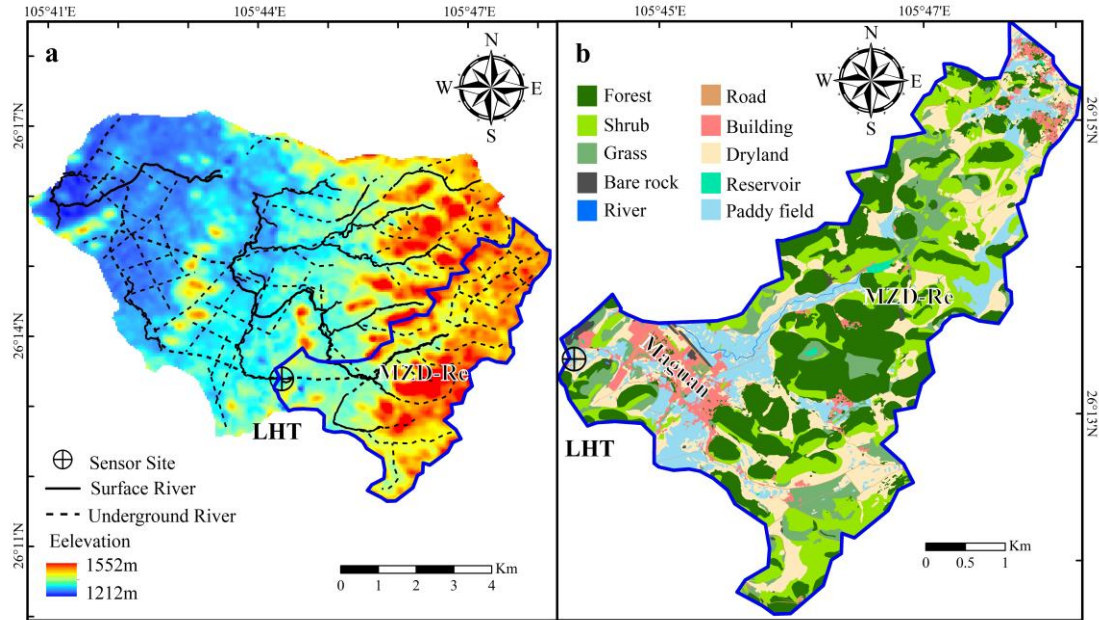


Figure 1. (a) Topographic and hydrological flow pathways of Houzhai Catchment and (b) land use in the Laoheitan sub-catchment, adapted from Yue et al., 2019. The blue line represents the surface area of the LHT catchment.

2.2 In situ sensors

Sensors were deployed around 100 m downstream of the LHT spring (Figure 1b). The nitrate ion-selective electrodes (NISE), which auto-compensate for Cl^- and temperature, were used from May 2016 to the end of October 2017. Sensor calibration has been previously reported (Yue et al., 2019). In brief, discrete stream water samples were collected manually at weekly or biweekly intervals, with additional samples collected during precipitation event periods using an autosampler at short intervals. A

linear relationship between sensor $[\text{NO}_3^- - \text{N}]$ and laboratory-measured $[\text{NO}_3^- - \text{N}]$ from discrete samples was used to enable a time interval calibration. Additionally, the uncertainty (μC) of the time interval calibration was also evaluated and ranged from 0.25 to 0.37 mg/L (Yue et al., 2019). Hydro-chemistry parameters (including temperature T, electrical conductivity EC, pH, and dissolved oxygen DO) were continuously measured at the spring outlet using a multi-parameter probe (Aqua TROLL 600), calibrated approximately monthly. For online discharge monitoring, Hobo in-situ pressure transducers were used for the measurement of water level and Q was calculated using the stage-discharge relationship at the same location as the NISE (Zhang et al., 2021). All in-situ sensors measured at 15-minute intervals. Precipitation data were collected by a meteorological station in LHT.

2.3 Hysteresis indices calculation

Hysteretic patterns use hysteresis indices (HI) to quantify the shape, size and direction of hysteretic loops of C and Q. The magnitude of HI can therefore indicate levels of variation between the rising and falling limbs. Generally, one rainfall event was defined as a hydrological response to rainfall, which resulted in a well-defined Q peak comprised of a rising and falling limb, with an increase by at least 20 % of base flow (Lloyd et al., 2016b). However, Q during the falling limb did not always recover to pre-event base flow before a subsequent rising limb was initiated by rainfall and in such cases was defined as another rainfall event (Lloyd et al., 2016b). To compare all events together, the concentration and Q were normalized using the following equations (Neal et al., 2012):

$$Q_{i, \text{norm}} = \frac{Q_i - Q_{\min}}{Q_{\max} - Q_{\min}} \quad (1)$$

$$C_{i, norm} = \frac{C_i - C_{min}}{C_{max} - C_{min}} \quad (2)$$

where Q_i/C_i is discharged/concentration at timestep i , Q_{max}/C_{max} and Q_{min}/C_{min} are the maxima and minimum discharge/concentration during any individual rainfall event, respectively. $Q_{i, norm}/C_{i, norm}$ is the normalized discharge/concentration, ranging from 0 to 1.

To quantify the relationship between Q and C , Lloyd et al (2016a) calculated the variation of normalized C at the corresponding level of Q in rising and falling limb with different intervals of Q (10 % ~ 100 %) using equation (3) and defined the hysteresis index (HI ranging from -1 to 1) as the average value of HI_j :

$$HI_j = C_{j, norm, rising} - C_{j, norm, falling} \quad (3)$$

where $C_{j, norm, rising}$, $C_{j, norm, falling}$ are $C_{j, norm}$ at measuring point $Q_{j, norm}$ of the rising and falling limb, in this study $j=10\%, 20\%, 30\%, \dots, 90\%$. Some of the $C_{j, norm, rising}$ data is generated by linear regression of C_i using two adjacent measurements at 10% intervals of Q_i on both the rising and falling limbs (Vaughan et al., 2017). Therefore, when the solute concentration of the rising limb is higher than in the falling limb at the same normalized Q , HI is a positive value and suggests the relationship between C and Q is clockwise. Conversely, a negative HI value signals anticlockwise hysteresis. HI values in the figure-of-eight can be either positive or negative (Lloyd et al., 2016b).

2.4 Flushing index calculation

To understand better the variation of solute concentrations during rainfall events, a flushing index (FI) was used for further characterization (Butturini et al., 2008; Vaughan et al., 2017):

$$FI = C_{Q peak, norm} - C_{initial, norm} \quad (4)$$

where $C_{Q peak, norm}$ and $C_{initial, norm}$ are the normalized solute concentrations at the point

of peak Q and the onset of the rainfall event, respectively. This index ranges from -1 to 1 and is equal to the slope of the line that intersects the first normalized solute concentration measured in each rainfall event and the normalized solute concentration at peak Q. A positive value indicates higher concentration, or flushing effect, in the rising limb, and a negative value suggests a decreased concentration, or dilution effect, in the rising limb.

2.5 Principal component analysis

PCA is one of the most successful statistical methods for factor analysis to reduce large dimensionality to smaller intrinsic dimensionality. This method uses a linear technique to compute eigenvectors, corresponding to the eigenvalues, which can be used to reconstruct a large fraction of the variance of the original data. Generally, the first few eigenvectors or eigenvalues (> 1) can be interpreted as the principal components, which contribute to the vast majority of the system's characteristics. Thus, this method eliminated the correlation between evaluation indicators and greatly reduced the workload of indicator selection and calculation. Briefly, 12 parameters including antecedent characteristics (6), rainfall (4) and discharge characteristics (2), were analyzed to reduce dimensionality using PCA (Table 1). A Kaiser-Meyer-Olkin test for these parameters returned a value > 0.60 , confirming that the PCA was valid. Then, a polynomial fit analysis was used among nitrate, hydrochemistry parameters characteristics and PCs during event flow.

Table 1. Description of antecedent conditions, rainfall, discharge, nitrate and hydrochemistry parameters characteristics in an individual rainfall event

Category	Parameter	Description
Antecedent conditions ($i=3, 7$)	R_i	Total rainfall in the i day before the event (mm/ i day)
	T_i	Average temperature within i day before the event ($^{\circ}\text{C}$)
	SR_i	Average solar radiation within i day before the event (W/m^2)
Rainfall	R_{Tot}	Total rainfall during each event (mm)

	R_{Int}	Rainfall intensity (mm/h)
	R_{Dur}	Duration of rainfall (hour)
	E_{Dur}	Duration of event (hour)
Discharge	Q_{Max}	The maximum of Q during each event (m^3/s)
	Q_A	Water yield (Q/area) (mm)
Nitrate characteristics	C_{Max}	The maximum of $[NO_3^- - N]$ during each event (mg/L)
	C_{Avg}	Average $[NO_3^- - N]$ during each event (mg/L)
	C_{Range}	Range of $[NO_3^- - N]$ during each event (mg/L)
	$\Delta C_{Start-End}$	$[NO_3^- - N]$ difference between the start and end of event
	F_A	Nitrate yield (flux/area) (kg/km^2)
	F_{Int}	Nitrate flux intensity (kg/h)
	HI	Hysteresis index
	FI	Flushing index
Hydrochemistry parameters	T_{Avg}	Average T during each event ($^{\circ}C$)
	EC_{Avg}	Average Conductivity (EC) during each event ($\mu s/cm$)
	pH_{Avg}	Average pH during each event (mg/L)
	DO_{Avg}	Average DO during each event (mg/L)

249 3 Results

250 3.1 Time series of nitrate-N concentration and discharge

251 Observations spanned a wet-dry-wet season cycle, and $[NO_3^- - N]$ responded to
252 precipitation and resulting variations in Q (Figure 2). $[NO_3^- - N]$ ranged from 1.4 to
253 12.4 mg/L at this site, with average and median values of 5.2 ± 1.4 and 5.1 mg/L,
254 respectively (Figure 2a). Most $[NO_3^- - N]$ maxima were observed during rainfall events
255 occurring earlier in the wet season and periods soon after fertilizer applications, with
256 concentrations exceeding both WHO drinking water standards (11.3 mg/L-N) and
257 China-specific standards (10 mg/L-N). Water Q ranged from 50 to 2536 L/s with mean
258 and median values of 234.3 and 223.2 L/s, respectively (Figure 2b). Compared to the
259 annual variation, $[NO_3^- - N]$ was higher during the wet season 2017 (5.6 ± 1.8 mg/L)
260 than in the wet season 2016 (4.8 ± 1.4 mg/L). Furthermore, $[NO_3^- - N]$ during the wet
261 season 2017 was higher than in the dry season 2016 (5.1 ± 0.6 mg/L) and decreased

until the intensive rainfall at the beginning of August 2017 (Figure 2a).

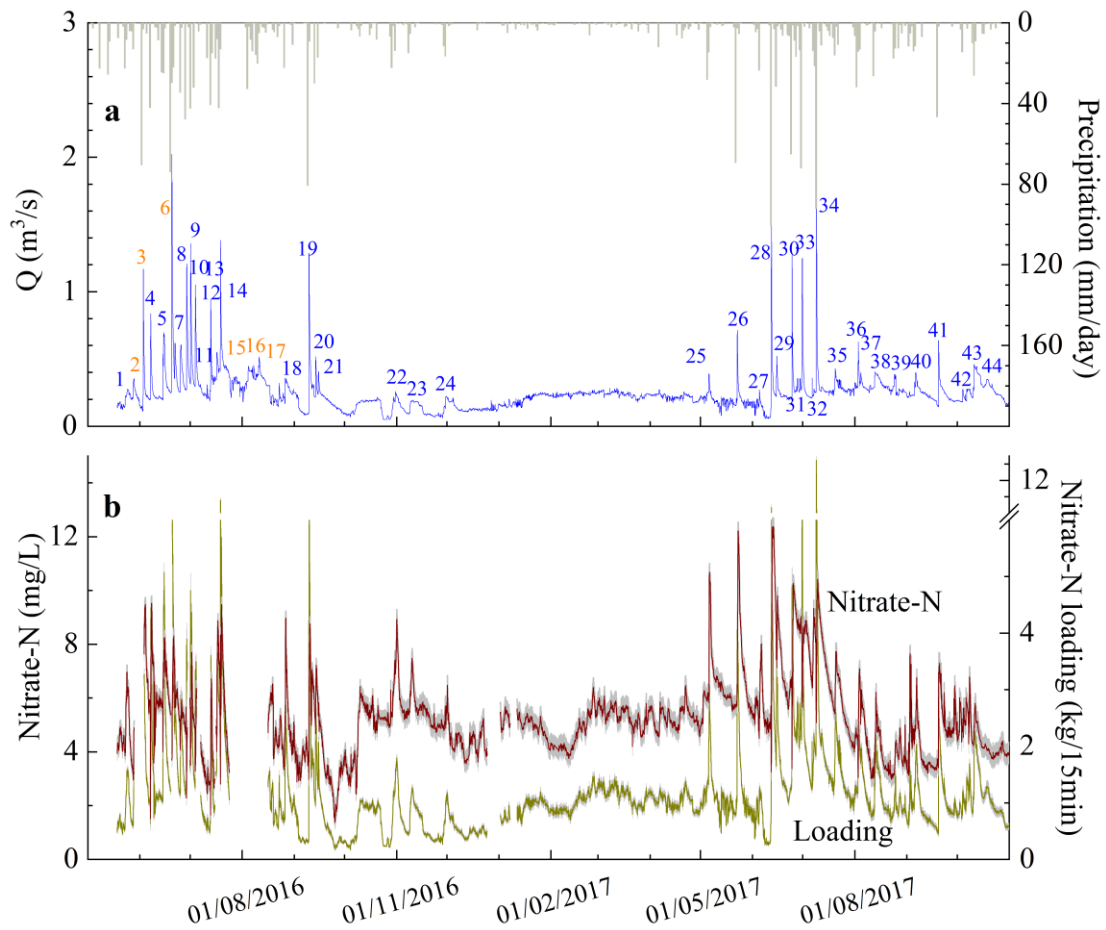


Figure 2 (a) time series of Q and precipitation (numbers represent the rainfall event, numbers with orange color represent events with missing sensor data) (Yue et al., 2019); (b) Time series of nitrate-N concentration and loading (the shaded light gray area associated with $[\text{NO}_3^- - \text{N}]$ represents the uncertainty of calibration).

A total of 44 rainfall events with complete hydrographs and rainfall more than 10 mm, which generated discharge higher than the base flow of at least 20 %, were extracted from the study time series (Figure 2b). The total rainfall associated with all 44 events was 1687 mm, which accounted for 74% of all rainfall during the study period, 3 events in the dry season (63 mm), 21 events during the wet season in 2016 (840 mm)

and 20 events during the wet season in 2017 (785 mm). The total duration of rainfall that resulted in defined event hydrographs accounted for 26.3% of the study period. Six rainfall events, at the beginning of the studied period (Figure 2a), were incomplete due to missing nitrate-N sensor data caused by a loss of power to the sensor or discontinuity in the sensor records because of maintenance. Consequently, only the characteristics of the remaining 38 rainfall events were analyzed. The duration of individual events ranged from 15 h to 334 h, including 18 events less than 50 h, 17 events between 50 h and 100 h and 9 events more than 100 h (Table S1). Three events (E22, E23 and E24) during the dry season with low discharge have recorded a duration of more than 200 h.

The average Q resulting from individual rainfall events ranged from 150 to 793 L/s. The nitrate-N loading and Q attributed to all rainfall events accounted for 33% and 34% of the study period, respectively. There were 19 events whereby the nitrate-N concentration at end of the defined event was lower than at the beginning of the event (Table S1, $\Delta C_{Start-End} > 0$). Although the nitrate-N concentration of event flow during the dry season was greater than part of the wet season, nitrate-N loading in the dry season was lower than during the wet season.

Generally, periods of 12 h precipitation can be categorized into different grades, e.g., moderate rain of 5 - 14.9 mm, heavy rain of 15 - 29.9 mm, storm rain of 30 - 69.9 mm and heavy storm rain of 70 - 139.9 mm (GB/T28592-2012). The N-Q relationships were determined during events of different rain intensity (Figure S1). The average $[\text{NO}_3^- - \text{N}]$ was 7.2 ± 1.5 mg/L during moderate rain ($n=2$), 5.5 ± 1.3 mg/L during heavy rain ($n=11$), 5.7 ± 1.5 mg/L during storm rain ($n=20$) and 8.6 ± 2.1 mg/L during heavy storm rain ($n=5$). Briefly, the variation of $[\text{NO}_3^- - \text{N}]$ was small during each moderate rainfall event, whereas relatively higher $[\text{NO}_3^- - \text{N}]$ variation was observed in moderate and heavy storm rainfall events.

3.2 Analysis of rainfall events and associated indices

The number of rainfall events, rainfall, HI and FI values associated with the three seasons of data collection are shown in Table S1. Overall, no rainfall events exhibited clockwise N-Q hysteresis relationships, while 10 rainfall events generated anticlockwise and negative HI values. N-Q relationships in the other 28 rainfall events resulted in a figure-of-eight hysteresis loop, including 8 clockwise figure-of-eight loop patterns and 20 anticlockwise figure-of-eight loop patterns. Therefore, 30 rainfall events (79%) show anticlockwise loop patterns.

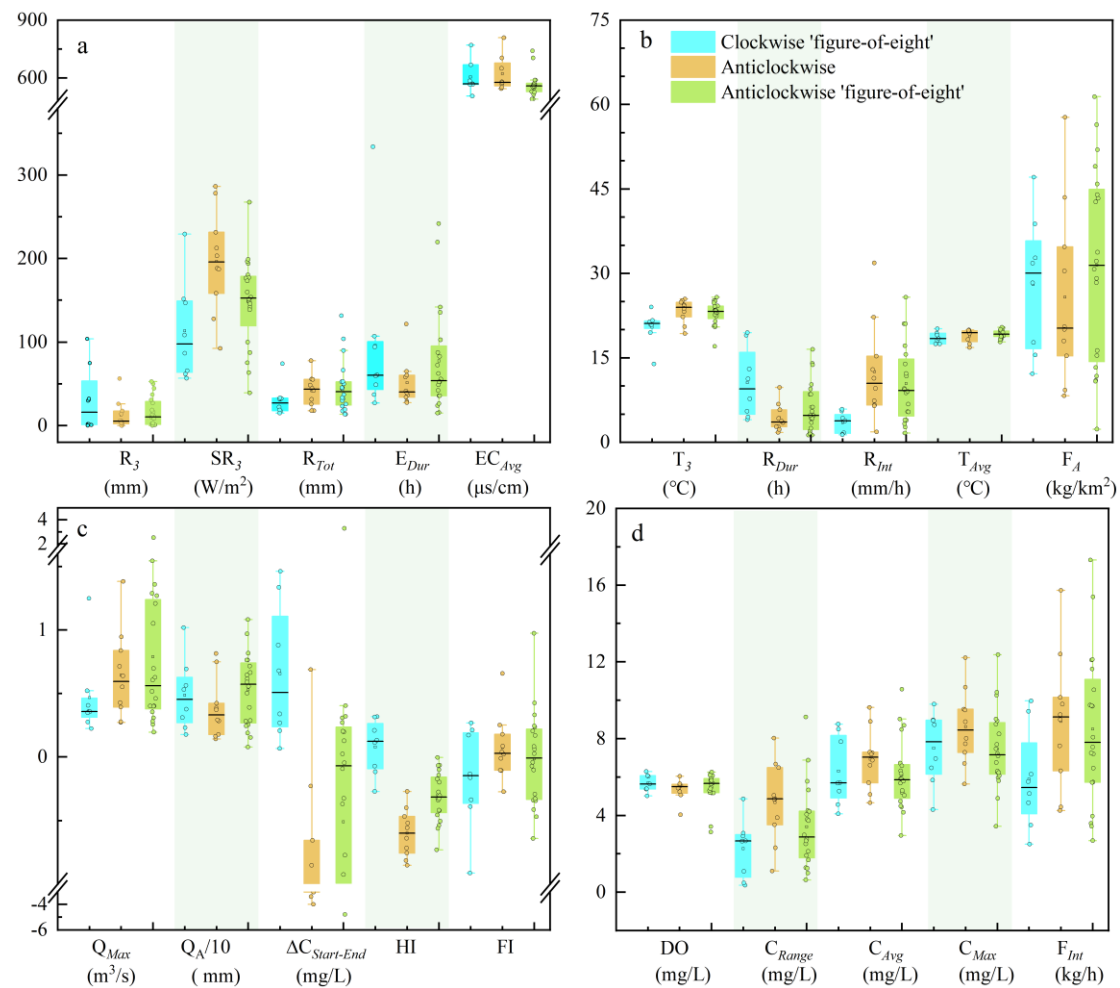


Figure 3 Boxplots the three days antecedent conditions (R_3 , SR_3 and T_3), rainfall condition (R_{Tot} , R_{Dur} , E_{Dur} and R_{Int}), water condition (Q_{Max} and Q_A), hydrochemistry (average of T, DO and EC; the average pH values were not shown owing to little

variance), nitrate characteristics ($\Delta C_{Start-End}$, C_{Range} , C_{Avg} , C_{Max} , F_A and F_{Int}), HI and FI in three N-Q patterns during rainfall events. The upper and lower edges of the box represent the 75th and 25th percentiles, respectively. The solid horizontal line in the box represents the median value. The branch gives the range of the data except for the outliers.

Greater variation of antecedent conditions was evident in ‘figure-of-eight’ events relative to events displaying anticlockwise hysteresis, particularly R_3 and SR_3 (Figure 3a). With respect to rainfall conditions, clockwise ‘figure-of-eight’ events showed lower R_{Tot} and R_{Int} , but higher R_{Dur} and E_{Dur} , resulting in low Q_{Max} , than the other two patterns (Figures 3a, b and c). Heavy and short duration rainfall events with short R_{Dur} and E_{Dur} , resulting in high R_{Tot} and low Q_A , would form an N-Q relationship with an anticlockwise loop. Although anticlockwise and anticlockwise ‘figure-of-eight’ have similar average R_{Tot} , moderate R_{Dur} and E_{Dur} in anticlockwise ‘figure-of-eight’ events resulted in most of them with high Q_A . Other characteristics, e.g., R_{Int} and Q_{Max} , showed more overlap between anticlockwise and anticlockwise ‘figure-of-eight’ events.

There was no significant variation of hydrochemistry parameters among the three hysteresis patterns (Figure 3), although a slightly lower EC_{Avg} was found in the anticlockwise ‘figure-of-eight’ pattern. Most of the events with a clockwise ‘figure-of-eight’ hysteresis loop showed a positive value of $\Delta C_{Start-End}$, indicating that nitrate was diluted, whereas negative values of $\Delta C_{Start-End}$ were found in all but one event with an anticlockwise loop (Figure 3c). In addition, the range of nitrate concentration during each event (C_{Range}) was highly variable for anticlockwise patterns (Figure 3d). The C_{Avg} and C_{Max} values were high in anticlockwise pattern events relative to the other two patterns (Figure 3d), which suggested high nitrate export intensity (F_{Int}) in the anticlockwise pattern.

FI values overlapped among the three hysteresis patterns identified (Figure 3b and 3c). There was no significant response between the flushing index (FI) and rainfall. For example, the mean rainfall in events with negative FI values ($46.5 \pm 23 \text{ mm}$, $n=8$) was higher than in events with positive FI values ($33.1 \pm 9.8 \text{ mm}$, $n=7$) during the 2016 wet season, whereas the converse was true for the 2017 wet season with high mean rainfall found in events with positive values ($47.6 \pm 27 \text{ mm}$, $n=11$). HI and FI in the 2017 wet season show a negative correlation ($R^2 = 0.43$, $P < 0.05$) but no correlation was observed for the other two seasons (Figure 4a).

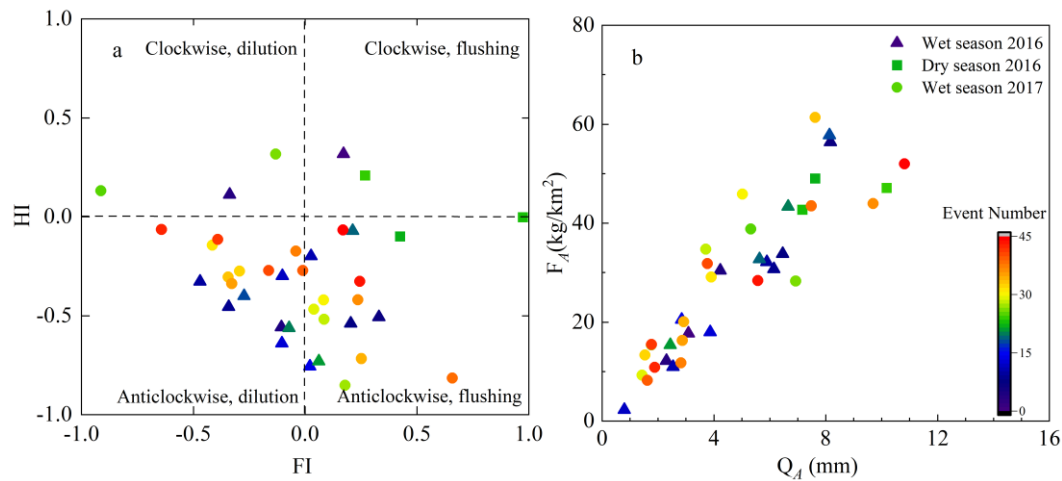


Figure 4 The relationship between HI and FI (a); water yield and nitrate yield (b).

3.3 Principal component analysis of rainfall events in karst spring

Results of the PCA identified four components that explained 82.0% of cumulative variance contribution (Figure 5). The first component explained 35.7% of the variance, with positive loading for the antecedent T and SR, attribution to the antecedent conditions. The second and third components had positive loading for R_{Tot} and antecedent rainfall (R_3 and R_7), explaining 19.6% and 16.2% of the variance, respectively. These two components can be classified as rain characteristics, which explained the variance equal to the first component. The fourth component explained 10.5% of the variance with positive loading for Q_A and R_{Dur} but negative to the R_{Int} ,

corresponding to the successive low rainfall events to promote the water yield.

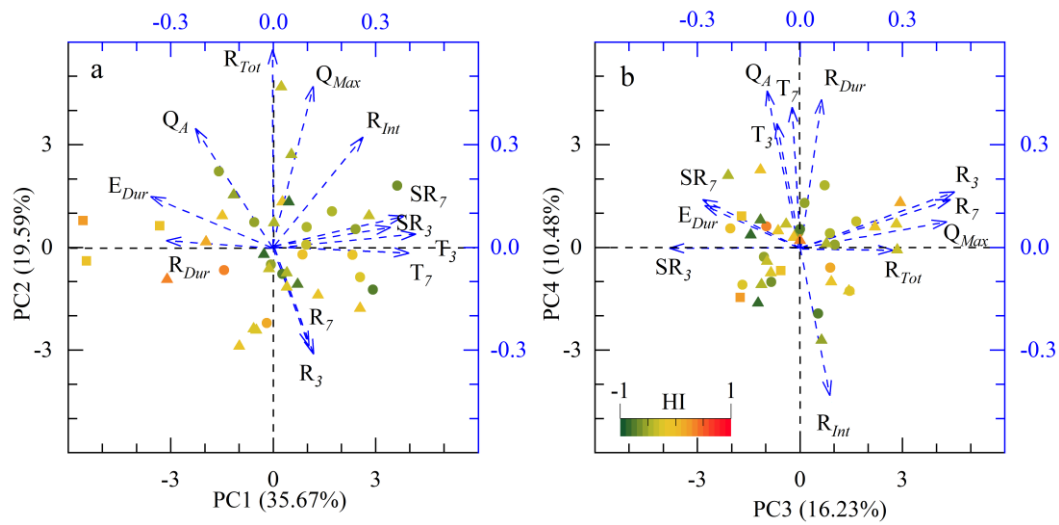


Figure 5 Principal component analysis for the 38 rainfall events (circle: wet season in 2016, square: dry season in 2016, triangle: wet season in 2017).

Table 2 Multiple linear regression for event nitrate and hydrochemistry characteristics

	PC1	PC2	PC3	PC4	R ²
F _A	-3.25**	6.91**	1.17	6.22**	0.81
F _{Int}	0.69**	1.01**	1.46**	0.05	0.58
HI	-0.07**	-0.04	0.02	0.04	0.25
FI	-0.06**	0.02*	-0.15**	-0.01	0.46
C _{Range}	0.24*	0.99**	0.09	-0.19*	0.52
ΔC _{Start-End}	-0.13	-0.32*	0.06	0.38	0.10
C _{Avg}	-0.04	0.23	0.65**	-0.26	0.26
C _{Max}	-0.05	0.49*	0.53*	-0.28	0.21
T _{Avg}	0.23**	-0.02	-0.12	0.31**	0.39
EC _{Avg}	-21.2**	-2.5	-28.5**	-26.4**	0.67
pH _{Avg}	-0.01	0.002	0.0004	0.005	-0.05
DO _{Avg}	-0.06	0.02	0.04	0.05	-0.09

* means $P < 0.05$, ** means $P < 0.01$

The multiple linear regression between nitrate characteristics and four PCs indicated the four PCs explained F_A, F_{Int}, C_{Range} and EC_{Avg} (more than 50%, Table 2), moderately explained FI and T_{Avg} (more than 30%) and explained HI, C_{Avg} and C_{Max} less

well (25%, 26% and 21%, respectively). The four PCs were unable to explain the hydro-chemical parameters pH_{Avg} and DO_{Avg} .

4 Discussion

4.1 Source availability and hydrological connectivity determined N-Q patterns

Changes in Q and $[\text{NO}_3^- - \text{N}]$ showed a rapid response to rainfall events in this karst spring. For example, peak Q increased more than 9-fold from the base flow level within 4 hours and recovered to baseline Q levels within the following two days (e.g., E6, E19, E34). This pattern of rapid response is typical of karst-dominated catchments because of the wide distribution of sinkholes and dual aquifers with low runoff coefficients that facilitate fast conduit flow (Chen et al., 2018; Huebsch et al., 2014), such that Q returns to base flow conditions more quickly than observed in non-karst catchments (Huebsch et al., 2014; Jiang et al., 2014). As such, $[\text{NO}_3^- - \text{N}]$ showed significant fluctuation and higher concentrations than observed in non-karst areas (Rose et al., 2018; Wollheim et al., 2017), particularly with rising concentration during the falling limb of hydrographs. This indicates high availability of nitrate in the catchment transported over distance to the monitoring site, and manifest as anticlockwise hysteresis. Anticlockwise hysteresis has been observed more common in agricultural catchments with high source availability than in urban and forested catchments (Miller et al., 2017; Vaughan et al., 2017), accumulated nitrate in soil from fertilizer application is likely to be a key factor in such observations.

Hydrological connectivity of catchment networks ranging from uplands hillslopes to the stream has been used to describe the event flow generation process; the landscape ‘wets-up’, approaching near saturation of soil and in turn facilitates increased subsurface and overland flow and associated solute transportation (McGuire and

McDonnell, 2010; Wang et al., 2023). Nitrate loading monitored in the catchment is a function of Q and mobilized sources that are delivered to receiving waters. Previous research has revealed that catchment groundwater, rainfall and soil water jointly controlled event flow (McGuire and McDonnell, 2010; Rose et al., 2018). Unlike non-karst catchments, stored water in the karst matrix is replaced by groundwater contributions to represent primary event flow during the early and later stages of an event (Chen et al., 2018; Zhang et al., 2021). Meanwhile, limited soil water from thin karstic soil would overlap with new water from rainfall via fast flow and Q increase gradually to peak as a result of the direct flow paths linking the surface to underground aquifer systems and enhance hydrological connectivity within the karst catchment during successive rainfall events.

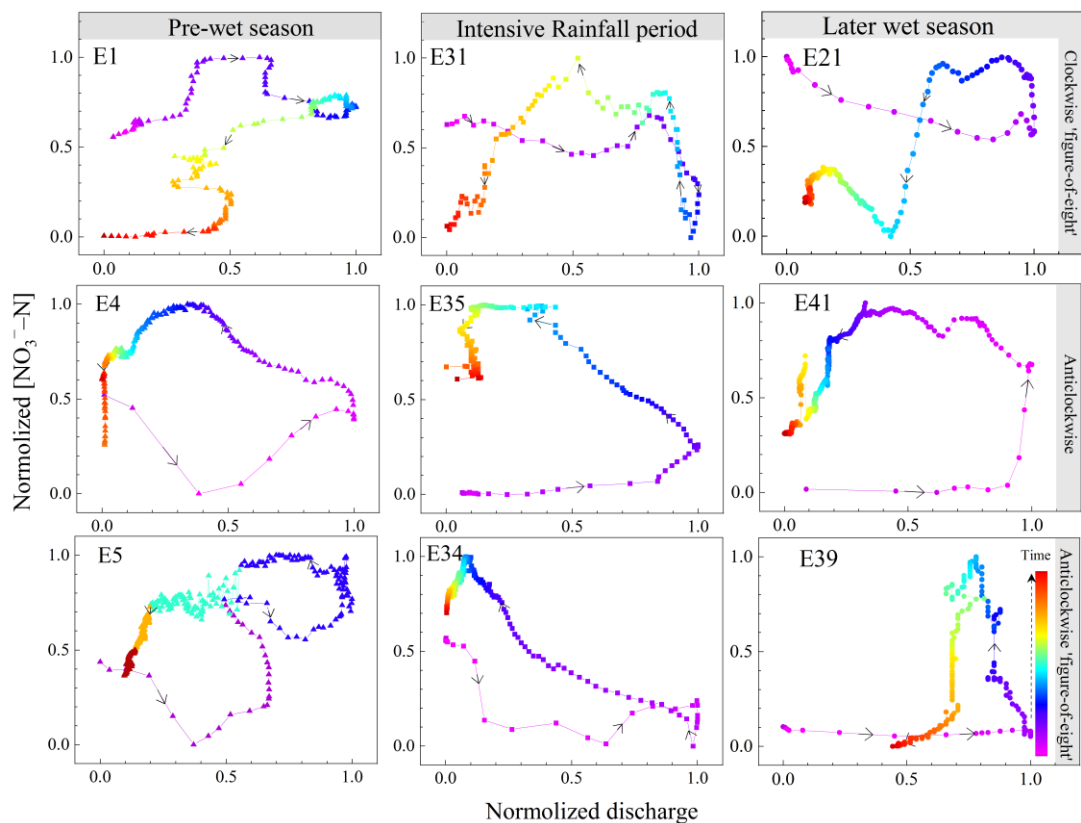


Figure 6 The three N - Q patterns in the pre-wet period (E1, E4 and E5), intensive rainfall (E31, E34 and E35) and later wet season (E21, E41 and E39).

To clearly show the three N-Q patterns of the three hysteresis patterns identified,

adjacent rainfall events during three periods with different hydrological connectivity are provided (Figure 6). Here, the N-Q pattern in the adjacent events (E1, 4 and 5) is accompanied by a change in hydrological connectivity. Although moderate R_{Tot} in these three events, the gradual increase in water yield (Table S1, Q_A) indicated hydrological connectivity has changed gradually from dry to wet, which shortened the nitrate transportation time and led to an increase in flushed nitrate being transported during event flow from epikarst. However, the low hydrological connectivity during the early wet season cannot effectively transport accumulated nitrate from the whole catchment. This limited transport resulted in the exported nitrate area being close to the monitored outlet and being influenced by the event's fast flow to form N-Q relationship with clockwise 'figure-of-eight' loop. Examples of such a response were recorded at the beginning and latter stages of the wet season (E1&E21) owing to source accumulation by nitrification and slowdown of growing usage.

With increases in hydrological connectivity, waters of relatively low nitrate concentration were transferred via fast flow with flushed nitrate sources from hillslopes with nature vegetation being transported over long distances to the monitored outlet during events, with particularly high nitrate concentrations recorded at the latter stage of event (Huebsch et al., 2014; Yue et al., 2019). Additionally, the dual flow system (fast and slow flows) can also shorten water and nitrate transport time in the heterogeneous karst to a greater extent than in non-karst systems and facilitate more efficient mixed solute transport from different land use found in the present study area (Yang et al., 2013; Zhang et al., 2021). Therefore, nitrate would be transported from near the monitored site and upper reaches area, manifest as N-Q pattern, particularly clockwise, 'figure-of-eight' during intensive rainfall period (e.g., E31) owing to a gradual increase in hydrological connectivity of the catchment.

Periods of intense rainfall occur in the catchment during the wet season, but nitrate loading contributions from rainfall are expected to be limited because the major species of nitrogen in rain is ammonium and easily adsorbed by soil (Zeng et al., 2020). Furthermore, nitrate concentration in rain is normally less than 1 mg/L and less than the lowest nitrate concentration in the wet season (Song et al., 2017; Zeng et al., 2020). Rather nitrate concentration during events was diluted by wet precipitation. Zhang et al. (2021) reported that the mean flow age on the rising limb was younger than the falling limb, revealing that the rising limb is more influenced by fast flow. The dilution effect was more clear during intensive rainfall events as the dominant fast flow with low nitrate concentration integrated with the slow flow with high nitrate concentration (Yue et al., 2019). For example, N-Q patterns displayed anticlockwise (e.g., E35) or ‘figure-of-eight’ with more anticlockwise hysteresis (e.g., E34), which is indicative of nitrate being sourced from areas far from the monitored outlet. Although nitrate concentration may decrease by dilution by multiple hydrological flushes following rainfall events (Figure 1), increased hydrological connectivity would enhance runoff generation and rapid hydrological transport, which resulted in a strong correlation between Q_A and F_A ($R^2 = 0.80$, $P < 0.01$) (Figure 4b). Therefore, effective source management activities should consider to intercepting or reducing source transportation during high hydrological connectivity periods. For example, nitrogen fertilizer application, e.g., fertilization level, time and types, should consider to reducing source availability during intensive rainfall periods. In addition, farming area should keep away from sinkholes or intercept agricultural overland flow to sinkholes to reduce nitrogen loss by the fast flow.

N-Q patterns in the latter stages of the wet season differed from those of intensive rainfall events, but were more similar to the pre-wet condition events, e.g., E21&E1,

E41&E4, E39&E5, indicating source availability and moderate hydrological connectivity controlling N-Q pattern in pre and latter wet season event flow. Source availability will increase due to decreased uptake of plants and low hydrological connectivity during the dry season, but nitrate produced by nitrification may also accumulate in storage in the epikarst under prolonged dry conditions (Rusjan et al., 2008). Positive and high FI values during the dry season with subsequent leaching and transport to receiving waters were driven by rainfall. The relatively low rainfall in the dry season is unlikely to leach all nitrate from the soil layer but high FI values suggested a high flushing of a mixture of nitrate from the soil layer and base flow indicating that loading of accumulated nitrate cannot be ignored and may represent a major contributor.

Although in our study HI and FI showed a negative relationship, chronological order was not observed in the two wet seasons (Figure 4a). This indicated that the temporal variations in nitrate source and the extent of hydrological connectivity to the karst aquifer system may vary and be further influenced by microbial activities and fertilizer application (Duncan et al., 2017; Rue et al., 2017; Yue et al., 2020).

4.2 Antecedent conditions and source availability determined nitrate loading during rainfall event in karst spring

Four PCs provided a low level of explanation for nitrate characteristics (HI, C_{Avg} and C_{Max}) of the events, which indicated that other factors might control their observed behavior over time. For example, although antecedent R, SR and T were considered, PCA and MLR analysis cannot evaluate directly nitrate uptake by plants and nitrate production by nitrification and loss by denitrification in the epikarst system (Heffernan et al., 2012; Husic et al., 2020; Song et al., 2017). During the wet season, nitrate could be produced from soil organic nitrogen by microbial activities within the catchment and nitrogen inputs from agricultural activities. During rainfall events, multiple nitrate

sources with dynamically varying contributions caused the increase or decrease of nitrate concentration. Others have observed that fertilizer application and nitrate accumulation in soil were the major reason for high levels of nitrate-N (Lawniczak et al., 2016; Miller et al., 2017).

Multiple linear regression analysis suggested four PCs that provide a high level of explanation of nitrate export (F_A and F_{Int}) in the rainfall events considered in this study. High temperature and solar radiation, (SR_i and T_i), benefit plant growth, decreasing nitrogen source availability in farmland and wider catchment. However, in these antecedent conditions, soil water content would decrease and subsequently increase the rate of reactive nitrogen production via mineralization and nitrification (Li et al., 2021; Li et al., 2020). Therefore, two aspects played a reverse role in nitrogen source availability. The comprehensive effect in the present karst catchment showed the antecedent high temperature and solar radiation decreased nitrogen source availability, which can be observed from the negative contribution to the F_A (Table 2). In contrast, more R_{Tot} and successive rainfall events ‘wet up’ the catchment and therefore promote hydrological connectivity, resulting in rapid nitrate transport (Blaen et al., 2017). Finally, the high Q_A will increase nitrate-N yield (F_A) under high hydrological connectivity within the catchment.

The MLR among FI and PCs demonstrated that the antecedent conditions (PC1) is negative to FI, which means that the flushing effect would more obvious when nitrate accumulation followed low SR_i and T_i , e.g. rainy days. Therefore, accumulated nitrogen sources can be easier to form nitrate peaks before discharge peaks during the following events, which can be observed in events with positive HI values and long rainfall intervals, particularly in dry season. MLR indicated nitrate loading was highly controlled by rainfall characteristics (PC2 and PC4) in turn influencing highly variable

Q and nitrate-N export. Overall, antecedent conditions and source availability are key factors influencing nitrate loading, observed in other study areas (Ford et al., 2019; Husic et al., 2019; Wymore et al., 2016).

Additionally, 74% of observed rainfall generated only 34% of event flow, thus the buffering capacity of the epikarst can influence HI, C_{Avg} and C_{Max} (Zhang et al., 2017), given that 74% of observed rainfall generated only 34% of event flow. There were more event flows with $HI < 0$ indicating the $[NO_3^- - N]$ during the falling limb may be receding slower than Q. This lag in the decline of $[NO_3^- - N]$ may be important due to the buffering capacity of the epikarst. However, $[NO_3^- - N]$ may remain elevated for longer periods than the defined event hydrograph because hydrological connectivity and source transport may be interrupted after rainfall events (Bowes et al., 2015; Rue et al., 2017). Miller et al. (2017) found that base flow (with a base flow ratio of 69%) provided a major contribution to nitrate export (89%) from groundwater supply. Although the well-developed karst aquifer system in upper reaches resulted in a low base flow ratio (7.3%), the middle reaches plains of the studies sites showed a moderate base flow ratio (41.4%) (Zhang et al., 2016b), which suggests that the karst matrix was the nitrate reservoir and regulated the chronic of N pollution (Yue et al., 2019). Thus, it is likely that nitrate dynamics or loading during base flow stored in the karst matrix may be a major driving factor for karst N transport and cannot be underestimated in the present study area (Chen et al., 2018).

Although the high nitrate concentration can be observed in the present study, the major chemical components cations and ions during event flow are Ca^{2+} , Mg^{2+} and HCO_3^- , SO_4^{2-} , respectively (Qin et al., 2020), which contributed to the variation of EC and were controlled by the water-rock interaction in karst area (Pratama et al., 2021; Yang et al., 2013). Similar to FI, PCs provide a negative contribution to EC_{Avg} ,

exhibiting that the dilution effect of rainfall on the chemical components in the fast hydrological karstic system is more obvious than in the non-karst areas (Trudeau and Richardson, 2016). Meanwhile, other hydro-chemical parameters (T_{Avg} , pH_{Avg} , DO_{Avg}) presented more complex than non-karst areas owing to energy transmission and buffer capacity of epikarst (Cheng et al., 2019; Pratt and Chang, 2012).

5. Conclusion

This study used high-frequency nitrate and water level sensor technology in a typical Chinese karstic agricultural area. Rainfall events and their characteristics were extracted from the study period and analyzed by PCA and other indices, including FI and HI, to understand the mechanisms of nitrate export from the karst agricultural area. The results indicated that heavy storm rainfall results in greater $[NO_3^- - N]$ in the event flow. PCA provided further insights regarding event characteristics with four PCs providing > 50% explanation of the variation of nitrate loading and amplitude during rainfall events (F_A , F_{Int} and C_{Range}). However, these four PCs poorly described nitrate concentrations (HI , C_{Avg} and C_{Max}), indicating these characteristics may be influenced more by nitrate transformation and source availability than these PCs. Antecedent conditions and rainfall characteristics determined the hydrological connectivity of catchment, which enabled water storage in the karst aquifer to transport nitrate over a long distance. The more rapid hydrological connectivity in karst landscapes coupled with high nitrogen source availability during the wet season determined N-Q patterns resembling ‘figure-of-eight’, particularly anticlockwise figure-of-eight loop patterns. Results from this study provide new information to further our understanding of the relationship between rainfall event characteristics and resulting nitrate characteristics (loading and concentration) in the karst area. The findings can therefore help to underpin the development of effective land management policy designed to limit

nutrient loss from land to water.

Declaration of competing interest

The authors declare that they have no known competing financial interests or personal relationships that could have appeared to influence the work reported in this paper.

Acknowledgments

The authors would like to thank for the anonymous reviewers' highly constructive suggestions and to acknowledge funding from the: Strategic Priority Research Program of Chinese Academy of Sciences [XDB40000000]; the UK Natural Environment Research Council, Grant/Award Number: NE/N007425/1; National Natural Science Foundation of China, Grant/Award Number: 42230509, 42073076. Sensor and hydrochemistry data for this site and others from these grants can be found at <https://doi.org/10.5285/f70596a1-0994-4b08-abab-0c9398af447d>. Authors thank Drs. Zhong-Jun Wang, Jie Zeng, Cai-Qing Qin for their help in sampling collection. Cai-Qing Qin, Yu-Chong Fu for their help in sampling collection. In addition, we would like to thank the Puding Karst Ecosystem Research Station for providing rainfall data. F-JY, S-LL, SW and DO designed the research objectives and interpreted the data and prepared the manuscript. F-JY carried out the field and laboratory work. F-JY, S-LL, SW, DO and PL conducted data analysis. XC, TP and CQL aided the interpretation of Karst hydrological and Karst Critical Zone. All of authors participated in discussion of the results.

References

Blaen, P.J., Khamis, K., Lloyd, C., Comer-Warner, S., Ciocca, F., Thomas, R.M., MacKenzie, A.R. and Krause, S. 2017. High-frequency monitoring of catchment nutrient exports reveals highly variable storm event responses and dynamic source zone activation. *J Geophys Res-Biogeosci* 122(9), 2265-2281.

577 Bowes, M.J., Jarvie, H.P., Halliday, S.J., Skeffington, R.A., Wade, A.J., Loewenthal, M., Gozzard, E.,
 578 Newman, J.R. and Palmer-Felgate, E.J. 2015. Characterising phosphorus and nitrate inputs to a
 579 rural river using high-frequency concentration-flow relationships. *Sci Total Environ* 511, 608-
 580 620.

581 Butturini, A., Alvarez, M., Bernal, S., Vazquez, E. and Sabater, F. 2008. Diversity and temporal
 582 sequences of forms of DOC and NO₃-discharge responses in an intermittent stream: Predictable
 583 or random succession? *J Geophys Res-Bioge* 113, G03016.

584 Carrey, R., Ballesté, E., Blanch, A.R., Lucena, F., Pons, P., López, J.M., Rull, M., Solà, J., Micola, N.,
 585 Fraile, J., Garrido, T., Munné, A., Soler, A. and Otero, N. 2021. Combining multi-isotopic and
 586 molecular source tracking methods to identify nitrate pollution sources in surface and
 587 groundwater. *Water Res* 188, 116537.

588 Chen, X., Zhang, Z.C., Soulsby, C., Cheng, Q.B., Binley, A., Jiang, R. and Tao, M. 2018. Characterizing
 589 the heterogeneity of karst critical zone and its hydrological function: An integrated approach.
 590 *Hydrol Process* 32(19), 2932-2946.

591 Cheng, Q., Chen, X., Tao, M. and Binley, A. 2019. Characterization of karst structures using quasi-3D
 592 electrical resistivity tomography. *Environ Earth Sci* 78: 285.

593 Duncan, J.M., Welty, C., Kemper, J.T., Groffman, P.M. and Band, L.E. 2017. Dynamics of nitrate
 594 concentration-discharge patterns in an urban watershed. *Water Resour Res* 53(8), 7349-7365.

595 Ford, D. and Williams, P.D. (2013) *Karst hydrogeology and geomorphology*, John Wiley & Sons.

596 Ford, W.I., Husic, A., Fogle, A. and Taraba, J. 2019. Long-term assessment of nutrient flow pathway
 597 dynamics and in-stream fate in a temperate karst agroecosystem watershed. *Hydrol Process*
 598 33(11), 1610-1628.

599 Gallo, E.L., Meixner, T., Aoubid, H., Lohse, K.A. and Brooks, P.D. 2015. Combined impact of catchment
 600 size, land cover, and precipitation on streamflow and total dissolved nitrogen: A global
 601 comparative analysis. *Global Biogeochemical Cycles* 29(7), 1109-1121.

602 Gao, Y. and Yu, G.-R. 2020. Regional coupled C-N-H₂O cycle processes and associated driving
 603 mechanisms. *Science China Earth Sciences* 63(9), 1227-1236.

604 Green, S.M., Dungait, J.A., Tu, C., Buss, H.L., Sanderson, N., Hawkes, S.J., et al. 2019. Soil functions
 605 and ecosystem services research in the Chinese karst Critical Zone. *Chem Geol.* 527:119107.

606 Gu, B., Ju, X., Chang, J., Ge, Y. and Vitousek, P.M. 2015. Integrated reactive nitrogen budgets and future
 607 trends in China. *Proceedings of the National Academy of Sciences* 112(28), 8792-8797.

608 Heffernan, J.B., Albertin, A.R., Fork, M.L., Katz, B.G. and Cohen, M.J. 2012. Denitrification and
 609 inference of nitrogen sources in the karstic Floridan Aquifer. *Biogeosciences* 9(5), 1671-1690.

610 Huebsch, M., Fenton, O., Horan, B., Hennessy, D., Richards, K.G., Jordan, P., Goldscheider, N., Butscher,
 611 C. and Blum, P. 2014. Mobilisation or dilution? Nitrate response of karst springs to high rainfall
 612 events. *Hydrol. Earth Syst. Sci.* 18(11), 4423-4435.

613 Husic, A., Fox, J., Adams, E., Ford, W., Agouridis, C., Currens, J. and Backus, J. 2019. Nitrate pathways,
 614 processes, and timing in an agricultural karst system: development and application of a
 615 numerical model. *Water Resour Res* 55(3), 2079-2103.

616 Husic, A., Fox, J., Adams, E., Pollock, E., Ford, W., Agouridis, C. and Backus, J. 2020. Quantification
 617 of nitrate fate in a karst conduit using stable isotopes and numerical modeling. *Water Res* 170,
 618 115348.

619 Jiang, Z.C., Lian, Y.Q. and Qin, X.Q. 2014. Rocky desertification in Southwest China: Impacts, causes,
 620 and restoration. *Earth-Sci Rev* 132, 1-12.

- Keesstra, S.D., Davis, J., Masselink, R.H., Casali, J., Peeters, E.T.H.M. and Dijkma, R. 2019. Coupling hysteresis analysis with sediment and hydrological connectivity in three agricultural catchments in Navarre, Spain. *J Soil Sediment* 19(3), 1598-1612.
- Kraus, T.E.C., O'Donnell, K., Downing, B.D., Burau, J.R. and Bergamaschi, B.A. 2017. Using paired in situ high frequency nitrate measurements to better understand controls on nitrate concentrations and estimate nitrification rates in a wastewater-impacted river. *Water Resour Res* 53(10), 8423-8442.
- Lang, M., Li, P. and Yan, X. 2013. Runoff concentration and load of nitrogen and phosphorus from a residential area in an intensive agricultural watershed. *Sci Total Environ* 458-460, 238-245.
- Lassaletta, L., Billen, G., Grizzetti, B., Garnier, J., Leach, A.M. and Galloway, J.N. 2014. Food and feed trade as a driver in the global nitrogen cycle: 50-year trends. *Biogeochemistry* 118(1), 225-241.
- Lawler, D.M., Petts, G.E., Foster, I.D.L. and Harper, S. 2006. Turbidity dynamics during spring storm events in an urban headwater river system: The Upper Tame, West Midlands, UK. *Sci Total Environ* 360(1-3), 109-126.
- Lawniczak, A.E., Zbierska, J., Nowak, B., Achtenberg, K., Grzeskowiak, A. and Kanas, K. 2016. Impact of agriculture and land use on nitrate contamination in groundwater and running waters in central-west Poland. *Environ Monit Assess* 188:172.
- Li, D., Wen, L., Xiao, K., Song, T. and Wang, K. 2021. Responses of soil gross nitrogen transformations to three vegetation restoration strategies in a subtropical karst region. *Land Degrad Dev* 32(8), 2520-2527.
- Li, S.-L., Liu, X., Yue, F.-J., Yan, Z., Wang, T., Li, S. and Liu, C.-Q. 2022. Nitrogen dynamics in the Critical Zones of China. *Progress in Physical Geography: Earth and Environment* 46(6), 869-888.
- Li, Z., Zeng, Z., Tian, D., Wang, J., Fu, Z., Zhang, F., Zhang, R., Chen, W., Luo, Y. and Niu, S. 2020. Global patterns and controlling factors of soil nitrification rate. *Global Change Biology* 26(7), 4147-4157.
- Liang, B., Liu, H., Quine, T.A., Chen, X., Hallett, P.D., Cressey, E.L., Zhu, X., Cao, J., Yang, S., Wu, L. and Hartley, I.P. 2020. Analysing and simulating spatial patterns of crop yield in Guizhou Province based on artificial neural networks. *Progress in Physical Geography: Earth and Environment* 45(1), 33-52.
- Liu, C.Q. (2007) Bio-geochemical processes and cycling of nutrients in the earth's surface: erosion of karstic catchment and nutrients cycling in Southwest China, Science Press, Beijing (In Chinese).
- Liu, W., Birgand, F., Tian, S. and Chen, C. 2021. Event-scale hysteresis metrics to reveal processes and mechanisms controlling constituent export from watersheds: A review. *Water Res* 200, 117254.
- Lloyd, C.E.M., Freer, J.E., Johnes, P.J. and Collins, A.L. 2016a. Technical Note: Testing an improved index for analysing storm discharge-concentration hysteresis. *Hydrol Earth Syst Sc* 20(2), 625-632.
- Lloyd, C.E.M., Freer, J.E., Johnes, P.J. and Collins, A.L. 2016b. Using hysteresis analysis of high-resolution water quality monitoring data, including uncertainty, to infer controls on nutrient and sediment transfer in catchments. *Sci Total Environ* 543, 388-404.
- Mahler, B.J., Valdes, D., Musgrove, M. and Massei, N. 2008. Nutrient dynamics as indicators of karst processes: Comparison of the Chalk aquifer (Normandy, France) and the Edwards aquifer (Texas, USA). *J Contam Hydrol* 98(1-2), 36-49.
- McGuire, K.J. and McDonnell, J.J. 2010. Hydrological connectivity of hillslopes and streams:

Characteristic time scales and nonlinearities. *Water Resour Res* 46:W10543.

Miller, M.P., Tesoriero, A.J., Hood, K., Terziotti, S. and Wolocks, D.M. 2017. Estimating discharge and nonpoint source nitrate loading to streams from three end-member pathways using high-frequency water quality data. *Water Resour Res* 53(12), 10201-10216.

Ming, X., Groves, C., Wu, X., Chang, L., Zheng, Y. and Yang, P. 2020. Nitrate migration and transformations in groundwater quantified by dual nitrate isotopes and hydrochemistry in a karst World Heritage site. *Sci Total Environ* 735, 138907.

Neal, C., Reynolds, B., Rowland, P., Norris, D., Kirchner, J.W., Neal, M., Sleep, D., Lawlor, A., Woods, C., Thacker, S., Guyatt, H., Vincent, C., Hockenhull, K., Wickham, H., Harman, S. and Armstrong, L. 2012. High-frequency water quality time series in precipitation and streamflow: From fragmentary signals to scientific challenge. *Sci Total Environ* 434, 3-12.

Opsahl, S.P., Musgrove, M. and Slattery, R.N. 2017. New insights into nitrate dynamics in a karst groundwater system gained from in situ high-frequency optical sensor measurements. *J Hydrol* 546, 179-188.

Ostrom, T.K. and Davis, A.P. 2019. Evaluation of an enhanced treatment media and permeable pavement base to remove stormwater nitrogen, phosphorus, and metals under simulated rainfall. *Water Res* 166, 115071.

Pratama, A.D., Dwiputra, D.S., Nurkholis, A., Haryono, E., Cahyadi, A., Agniy, R.F. and Adji, T.N. 2021. Factors affecting hydrochemistry of karst springs and their relationship to aquifer development. *Environmental Processes* 8(4), 1379-1413.

Pratt, B. and Chang, H. 2012. Effects of land cover, topography, and built structure on seasonal water quality at multiple spatial scales. *J Hazard Mater* 209-210, 48-58.

Pu, J.B., Yuan, D.X., He, Q.F., Wang, Z.J., Hu, Z.Y. and Gou, P.F. 2011. High-resolution monitoring of nitrate variations in a typical subterranean karst stream, Chongqing, China. *Environ Earth Sci* 64(7), 1985-1993.

Qin, C., Li, S.-L., Waldron, S., Yue, F.-J., Wang, Z.-J., Zhong, J., Ding, H. and Liu, C.-Q. 2020. High-frequency monitoring reveals how hydrochemistry and dissolved carbon respond to rainstorms at a karstic critical zone, Southwestern China. *Sci Total Environ* 714, 136833.

Rose, L.A., Karwan, D.L. and Godsey, S.E. 2018. Concentration-discharge relationships describe solute and sediment mobilization, reaction, and transport at event and longer timescales. *Hydrol Process* 32(18), 2829-2844.

Rue, G.P., Rock, N.D., Gabor, R.S., Pitlick, J., Tfaily, M. and McKnight, D.M. 2017. Concentration-discharge relationships during an extreme event: Contrasting behavior of solutes and changes to chemical quality of dissolved organic material in the Boulder Creek Watershed during the September 2013 flood. *Water Resour Res* 53(7), 5276-5297.

Rusjan, S., Brilly, M. and Mikos, M. 2008. Flushing of nitrate from a forested watershed: An insight into hydrological nitrate mobilization mechanisms through seasonal high-frequency stream nitrate dynamics. *J Hydrol* 354(1-4), 187-202.

Song, X., Gao, Y., Green, S.M., Dungait, J.A., Peng, T., Quine, T.A., Xiong, B., Wen, X. and He, N. 2017. Nitrogen loss from karst area in China in recent 50 years: An in-situ simulated rainfall experiment's assessment. *Ecol Evol* 7(23), 10131-10142.

Trudeau, M.P. and Richardson, M. 2016. Empirical assessment of effects of urbanization on event flow hydrology in watersheds of Canada's Great Lakes-St Lawrence basin. *J Hydrol* 541, 1456-1474.

- Vaughan, M.C.H., Bowden, W.B., Shanley, J.B., Vermilyea, A., Sleeper, R., Gold, A.J., Pradhanang, S.M., Inamdar, S.P., Levia, D.F., Andres, A.S., Birgand, F. and Schroth, A.W. 2017. High-frequency dissolved organic carbon and nitrate measurements reveal differences in storm hysteresis and loading in relation to land cover and seasonality. *Water Resour Res* 53(7), 5345-5363.
- Wang, Y., Lin, J., Wang, F., Tian, Q., Zheng, Y. and Chen, N. 2023. Hydrological connectivity affects nitrogen migration and retention in the land–river continuum. *J Environ Manage* 326, 116816.
- Wang, Z.-J., Li, S.-L., Yue, F.-J., Qin, C.-Q., Buckerfield, S. and Zeng, J. 2020. Rainfall driven nitrate transport in agricultural karst surface river system: Insight from high resolution hydrochemistry and nitrate isotopes. *Agri Ecosys Environ* 291, 106787.
- Wollheim, W.M., Mulukutla, G.K., Cook, C. and Carey, R.O. 2017. Aquatic nitrate retention at river network scales across flow conditions determined using nested in situ sensors. *Water Resour Res* 53(11), 9740-9756.
- Wymore, A.S., Coble, A.A., Rodríguez-Cardona, B. and McDowell, W.H. 2016. Nitrate uptake across biomes and the influence of elemental stoichiometry: A new look at LINX II. *Global Biogeochemical Cycles* 30(8), 1183-1191.
- Yang, P.H., Wang, Y.Y., Wu, X.Y., Chang, L.R., Ham, B., Song, L.S. and Groves, C. 2020. Nitrate sources and biogeochemical processes in karst underground rivers impacted by different anthropogenic input characteristics. *Environ Pollut* 265, 114835.
- Yang, P.H., Yuan, D.X., Ye, X.C., Xie, S.Y., Chen, X.B. and Liu, Z.Q. 2013. Sources and migration path of chemical compositions in a karst groundwater system during rainfall events. *Chinese Sci Bull* 58(20), 2488-2496.
- Yue, F.-J., Li, S.-L., Waldron, S., Wang, Z.-J., Oliver, D.M., Chen, X. and Liu, C.-Q. 2020. Rainfall and conduit drainage combine to accelerate nitrate loss from a karst agroecosystem: insights from stable isotope tracing and high-frequency nitrate sensing. *Water Res* 186, 116388.
- Yue, F.-J., Waldron, S., Li, S.-L., Wang, Z.-J., Zeng, J., Xu, S., Zhang, Z.-C. and Oliver, D.M. 2019. Land use interacts with changes in catchment hydrology to generate chronic nitrate pollution in karst waters and strong seasonality in excess nitrate export. *Sci Total Environ* 696, 134062.
- Zeng, J., Yue, F.-J., Li, S.-L., Wang, Z.-J., Qin, C.-Q., Wu, Q.-X. and Xu, S. 2020. Agriculture driven nitrogen wet deposition in a karst catchment in southwest China. *Agri Ecosys Environ* 294, 106883.
- Zhang, Q., Harman, C.J. and Ball, W.P. 2016a. An improved method for interpretation of riverine concentration-discharge relationships indicates long-term shifts in reservoir sediment trapping. *Geophys Res Lett* 43(19), 10215-10224.
- Zhang, R.R., Shu, L.C., Zhu, J.T., Yu, Z.B. and Jiang, P. 2016b. Storage and drainage characteristics of a highly heterogeneous karst aquifer in Houzhai Basin. *Groundwater* 54(6), 878-887.
- Zhang, X., Wu, Y. and Gu, B. 2015. Urban rivers as hotspots of regional nitrogen pollution. *Environ Pollut* 205, 139-144.
- Zhang, Z., Chen, X., Li, S., Yue, F., Cheng, Q., Peng, T. and Soulsby, C. 2021. Linking nitrate dynamics to water age in underground conduit flows in a karst catchment. *J Hydrol* 596, 125699.
- Zhang, Z., Chen, X. and Soulsby, C. 2017. Catchment-scale conceptual modelling of water and solute transport in the dual flow system of the karst critical zone. *Hydrol Process* 31(19), 3421-3436.

Figure captions

Figure 1. (a) Topographic and hydrological flow pathways of Houzhai Catchment and (b) land use in the Laoheitan sub-catchment, adapted from Yue et al., 2019. The blue line represents the surface area of the LHT catchment.

Figure 2 (a) time series of Q and precipitation (numbers represent the rainfall event, numbers with orange color represent events with missing sensor data) (Yue et al., 2019); (b) Time series of nitrate-N concentration and loading (the shaded light gray area associated with $[\text{NO}_3^- - \text{N}]$ represents the uncertainty of calibration).

Figure 3 Boxplots the three days antecedent conditions (R_3 , SR_3 and T_3), rainfall condition (R_{Tot} , R_{Dur} , E_{Dur} and R_{Int}), water condition (Q_{Max} and Q_A), hydrochemistry (average of T, DO and EC; the average pH values were not shown owing to little variance), nitrate characteristics ($\Delta C_{Start-End}$, C_{Range} , C_{Avg} , C_{Max} , F_A and F_{Int}), HI and FI in three N-Q patterns during rainfall events. The upper and lower edges of the box represent the 75th and 25th percentiles, respectively. The solid horizontal line in the box represents the median value. The branch gives the range of the data except for the outliers.

Figure 4 The relationship between HI and FI (a); water yield and nitrate yield (b).

Figure 5 Principal component analysis for the 38 rainfall events (circle: wet season in 2016, square: dry season in 2016, triangle: wet season in 2017).

Figure 6 The three N - Q patterns in the pre-wet period (E1, E4 and E5), intensive rainfall (E31, E34 and E35) and later wet season (E21, E41 and E39).

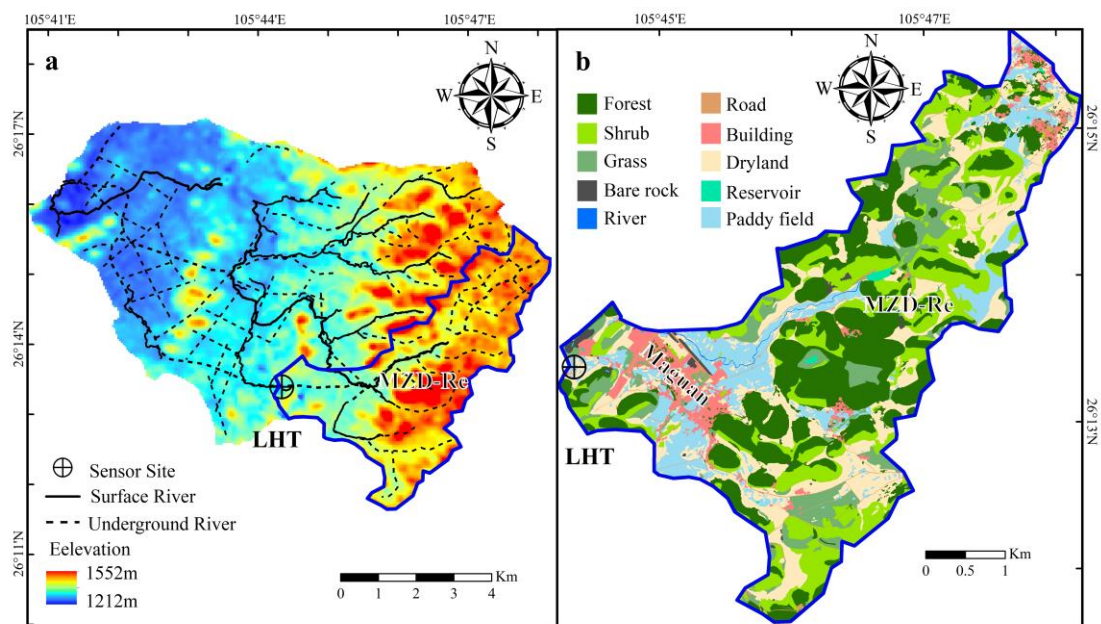


Figure 1.

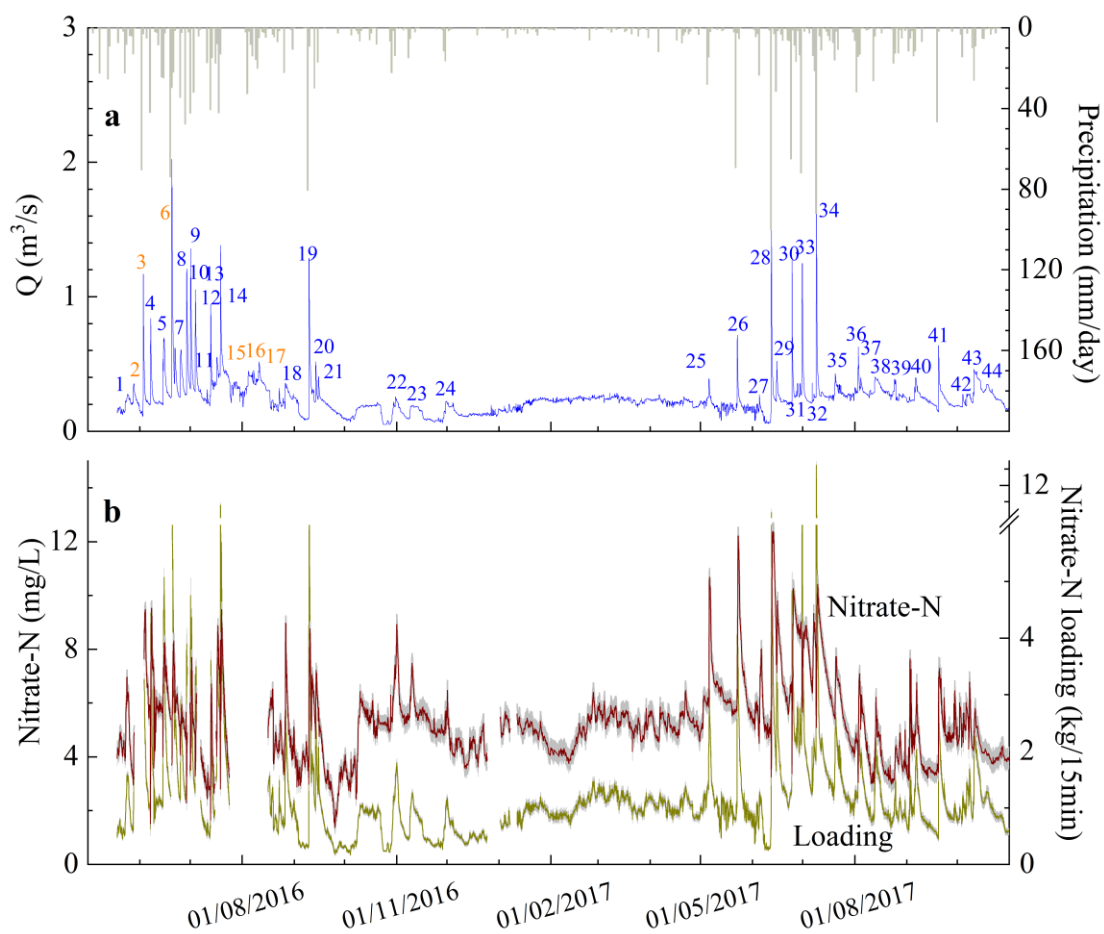


Figure 2

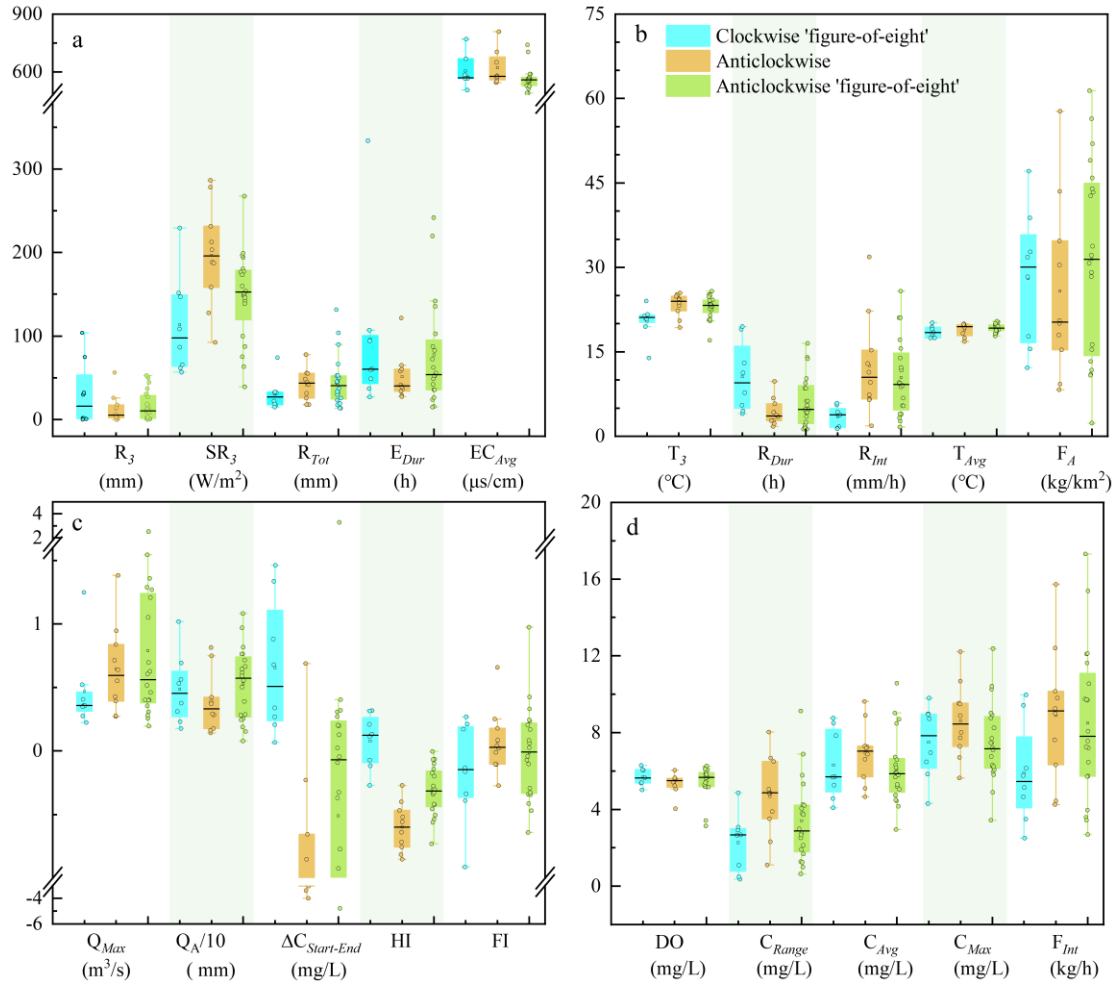


Figure 3

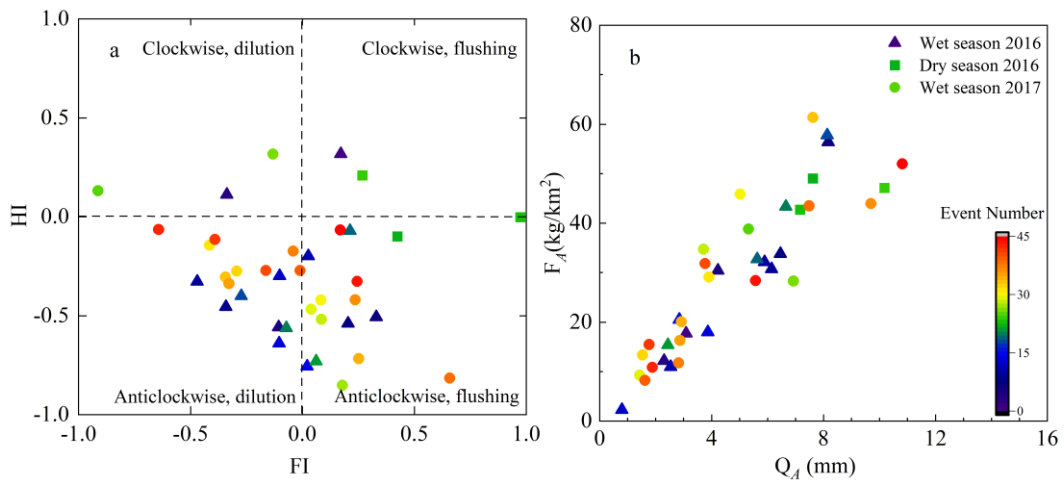


Figure 4

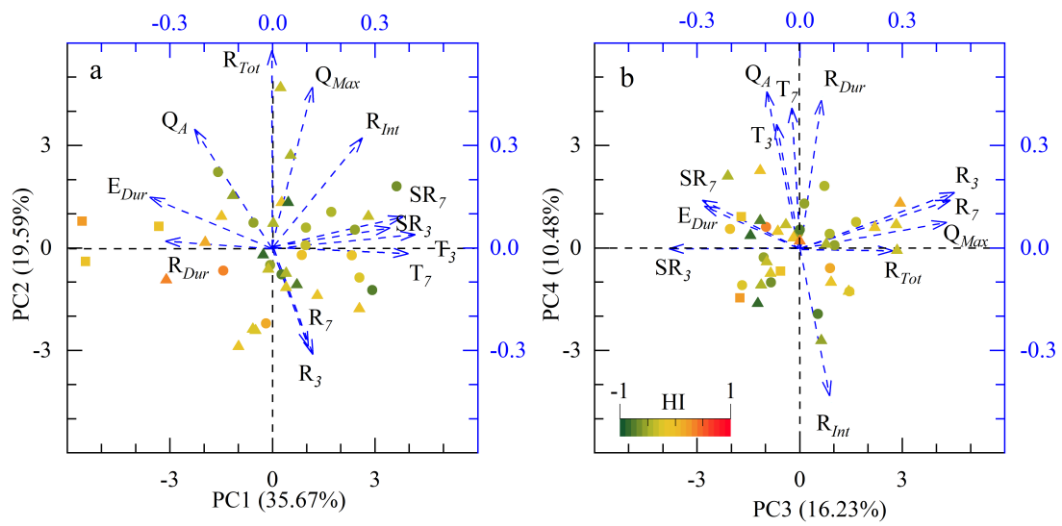


Figure 5

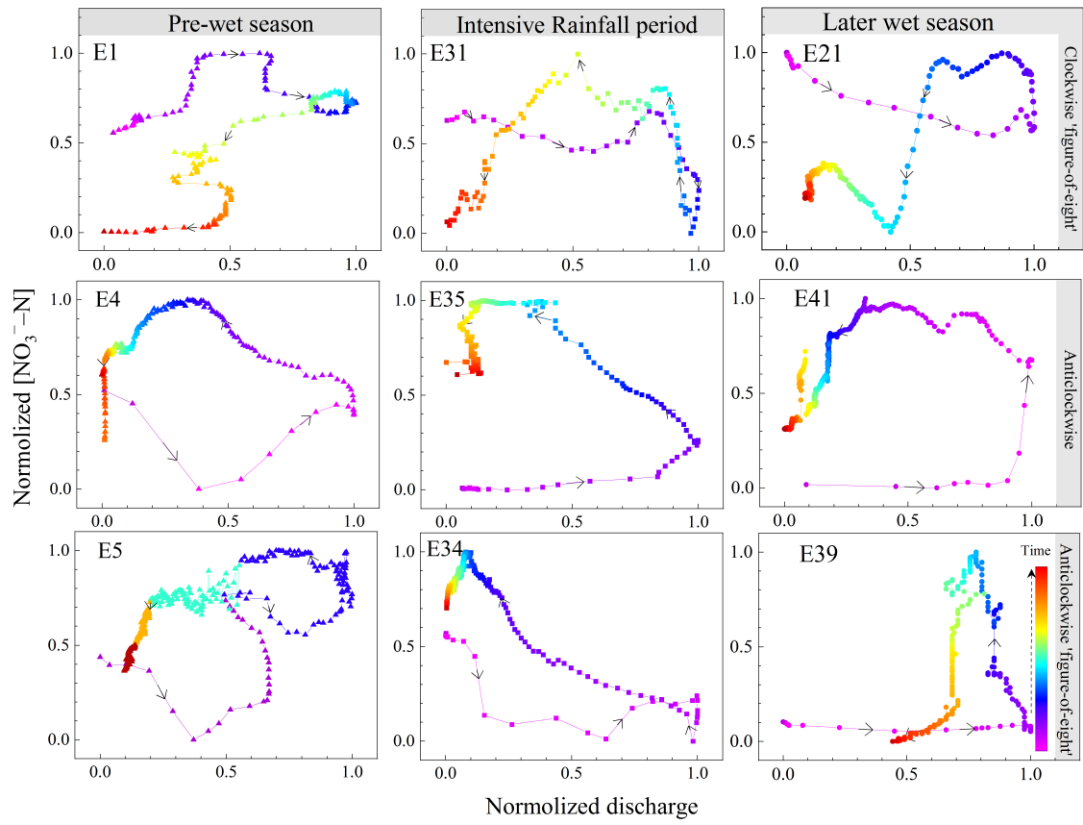


Figure 6

Table 1. Description of antecedent conditions, rainfall, discharge, nitrate and hydrochemistry parameters characteristics in an individual rainfall event

Category	Parameter	Description
Antecedent conditions ($i=3, 7$)	R_i	Total rainfall in the i day before the event (mm/ i day)
	T_i	Average temperature within i day before the event ($^{\circ}\text{C}$)
	SR_i	Average solar radiation within i day before the event (W/m^2)
Rainfall	R_{Tot}	Total rainfall during each event (mm)
	R_{Int}	Rainfall intensity (mm/h)
	R_{Dur}	Duration of rainfall (hour)
	E_{Dur}	Duration of event (hour)
Discharge	Q_{Max}	The maximum of Q during each event (m^3/s)
	Q_A	Water yield (Q/area) (mm)
Nitrate characteristics	C_{Max}	The maximum of $[\text{NO}_3^- - \text{N}]$ during each event (mg/L)
	C_{Avg}	Average $[\text{NO}_3^- - \text{N}]$ during each event (mg/L)
	C_{Range}	Range of $[\text{NO}_3^- - \text{N}]$ during each event (mg/L)
	$\Delta C_{Start-End}$	$[\text{NO}_3^- - \text{N}]$ difference between the start and end of event
	F_A	Nitrate yield (flux/area) (kg/km^2)
	F_{Int}	Nitrate flux intensity (kg/h)
	HI	Hysteresis index
	FI	Flushing index
Hydrochemistry parameters	T_{Avg}	Average T during each event ($^{\circ}\text{C}$)
	EC_{Avg}	Average Conductivity (EC) during each event ($\mu\text{S}/\text{cm}$)
	pH_{Avg}	Average pH during each event (mg/L)
	DO_{Avg}	Average DO during each event (mg/L)

Table 2 Multiple linear regression for event nitrate and hydrochemistry characteristics

	PC1	PC2	PC3	PC4	R ²
F _A	-3.25**	6.91**	1.17	6.22**	0.81
F _{Int}	0.69**	1.01**	1.46**	0.05	0.58
HI	-0.07**	-0.04	0.02	0.04	0.25
FI	-0.06**	0.02*	-0.15**	-0.01	0.46
C _{Range}	0.24*	0.99**	0.09	-0.19*	0.52
ΔC _{Start-End}	-0.13	-0.32*	0.06	0.38	0.10
C _{Avg}	-0.04	0.23	0.65**	-0.26	0.26
C _{Max}	-0.05	0.49*	0.53*	-0.28	0.21
T _{Avg}	0.23**	-0.02	-0.12	0.31**	0.39
EC _{Avg}	-21.2**	-2.5	-28.5**	-26.4**	0.67
pH _{Avg}	-0.01	0.002	0.0004	0.005	-0.05
DO _{Avg}	-0.06	0.02	0.04	0.05	-0.09

* means P < 0.05, ** means P < 0.01

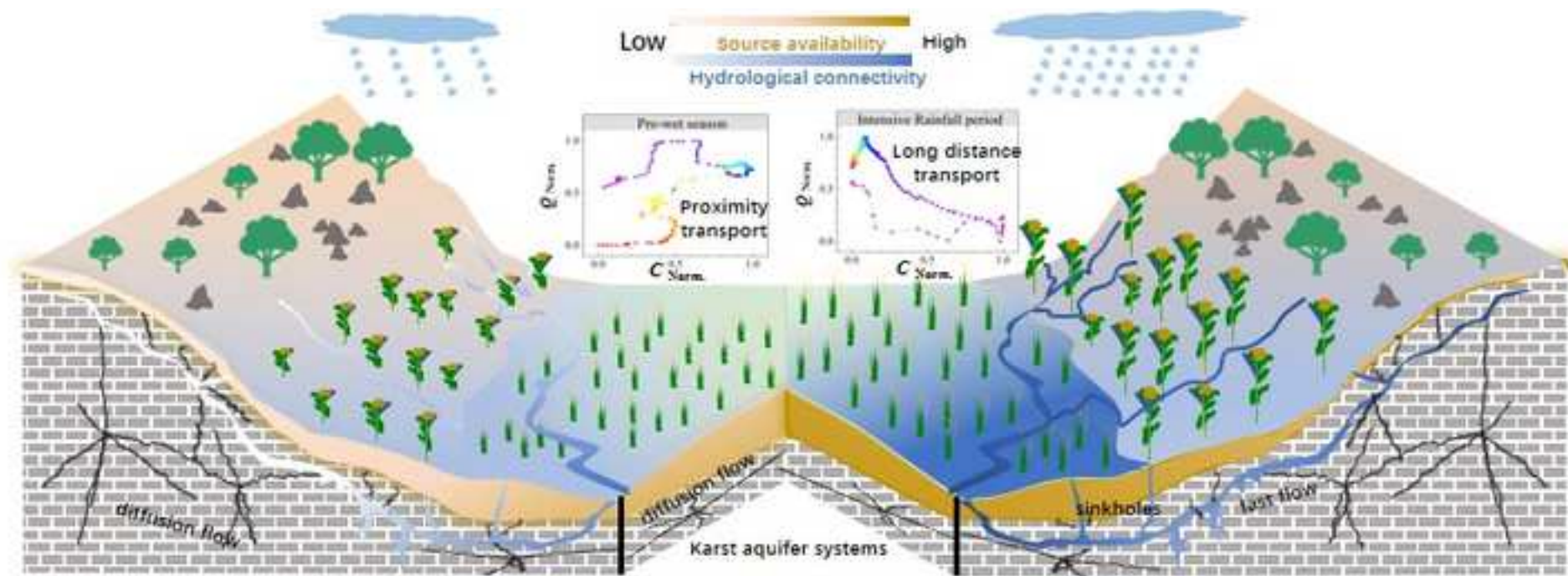


Figure 1

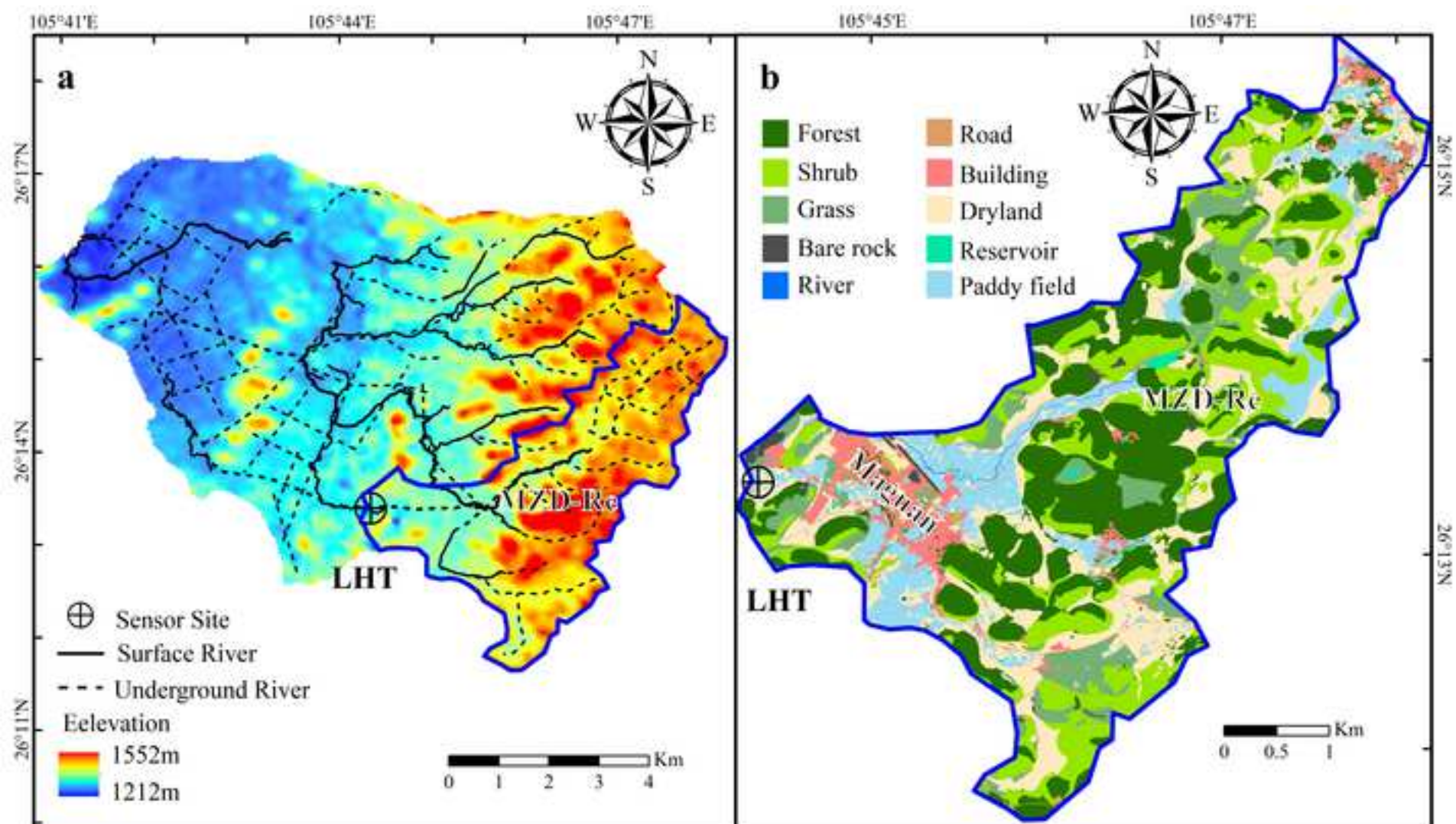


Figure 2

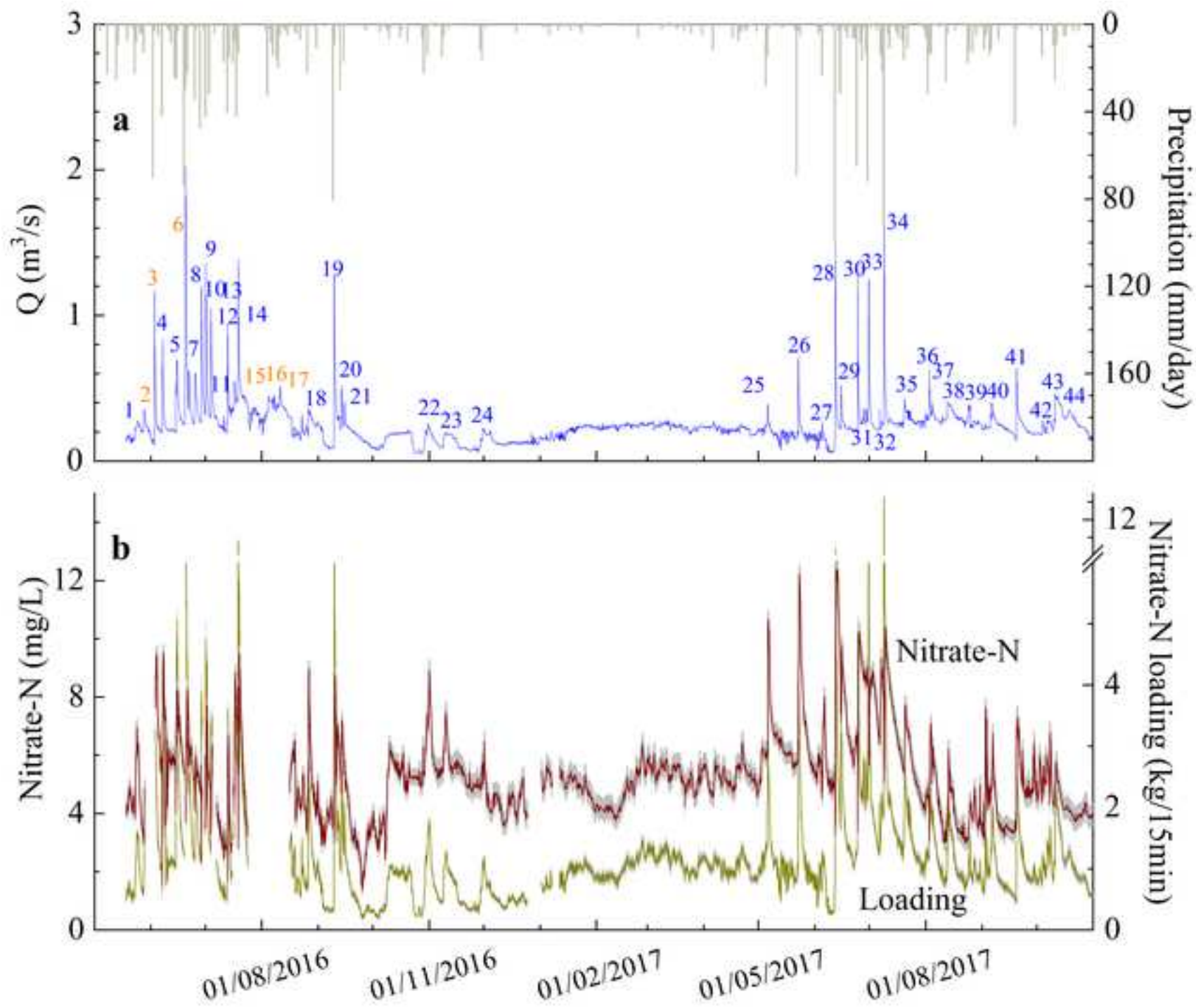


Figure 3

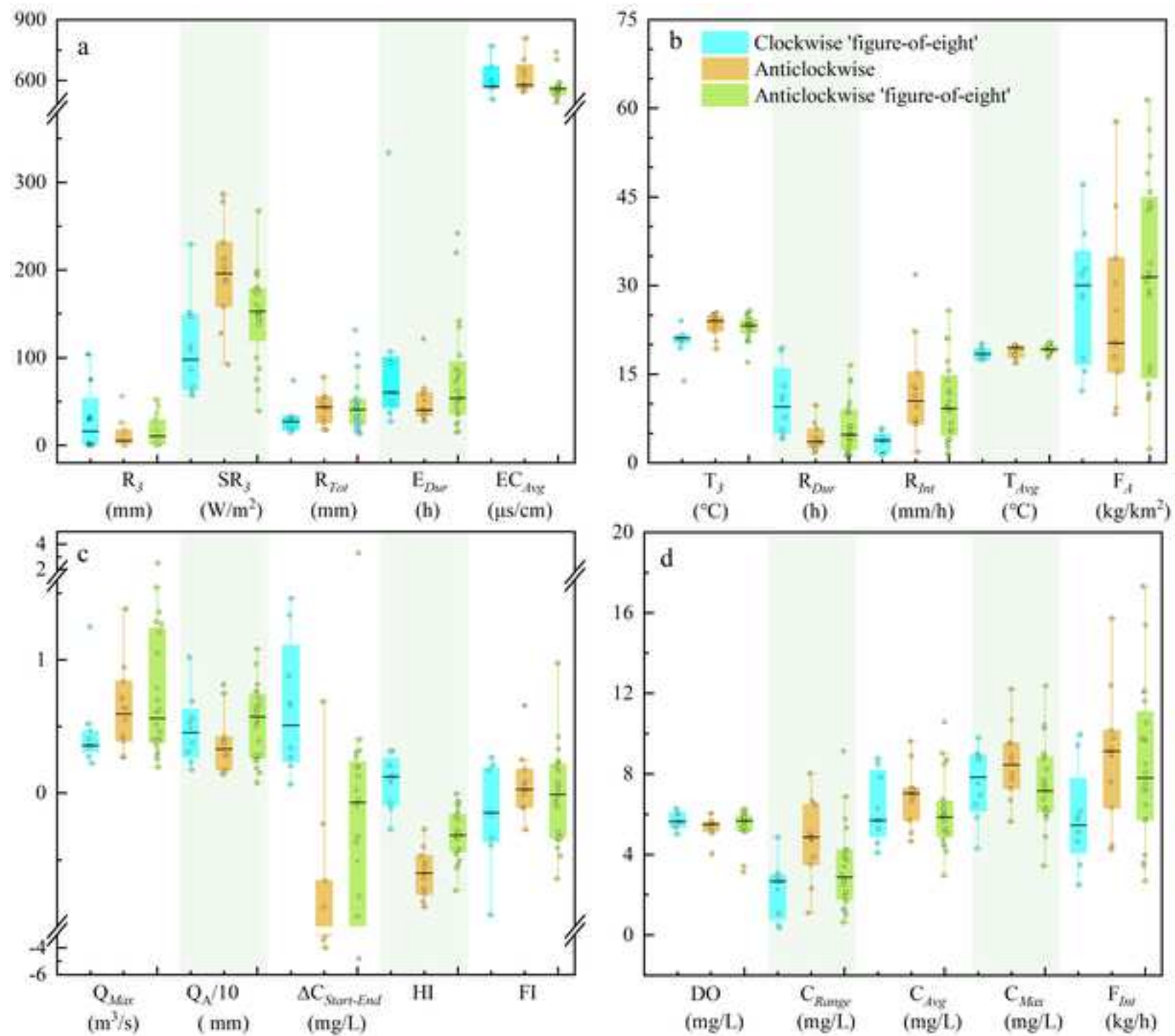


Figure 4

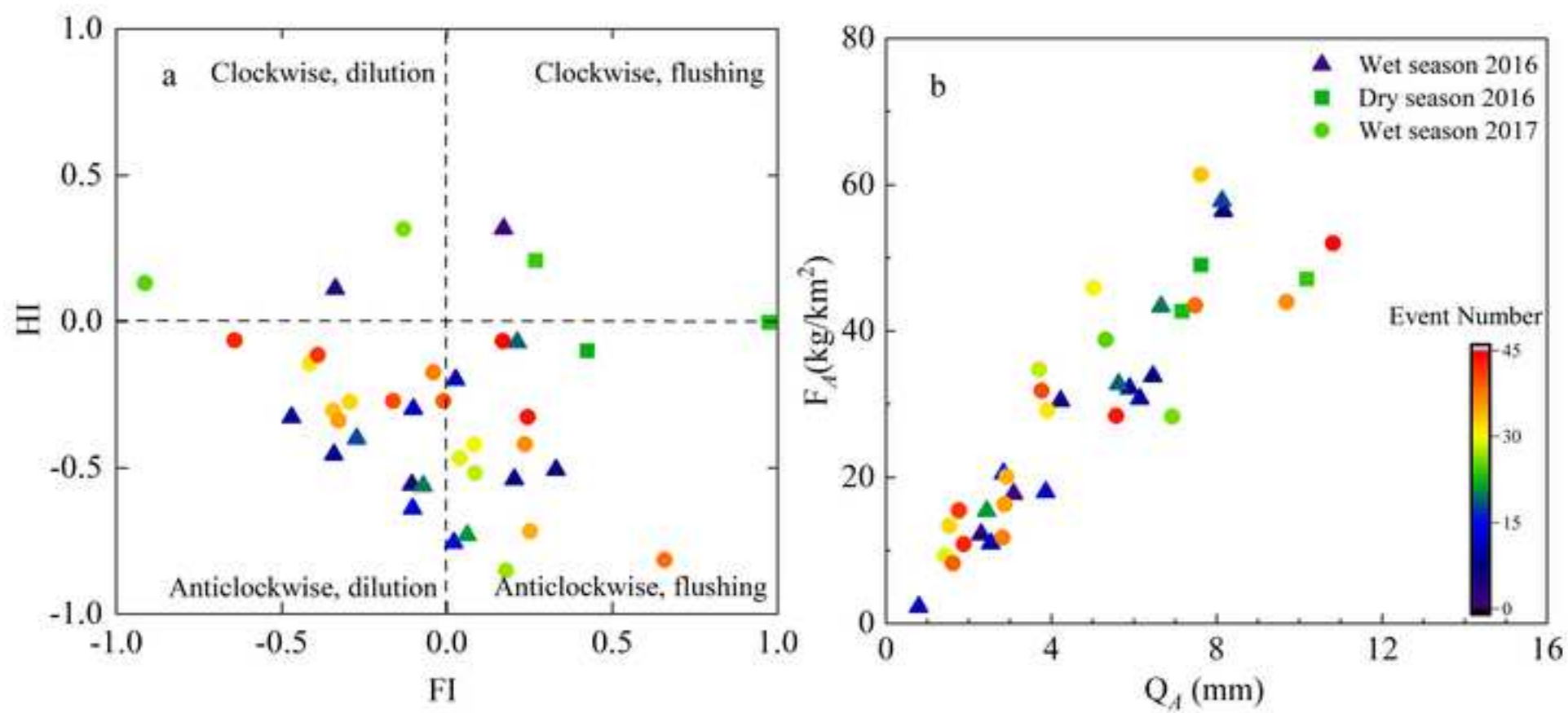


Figure 5

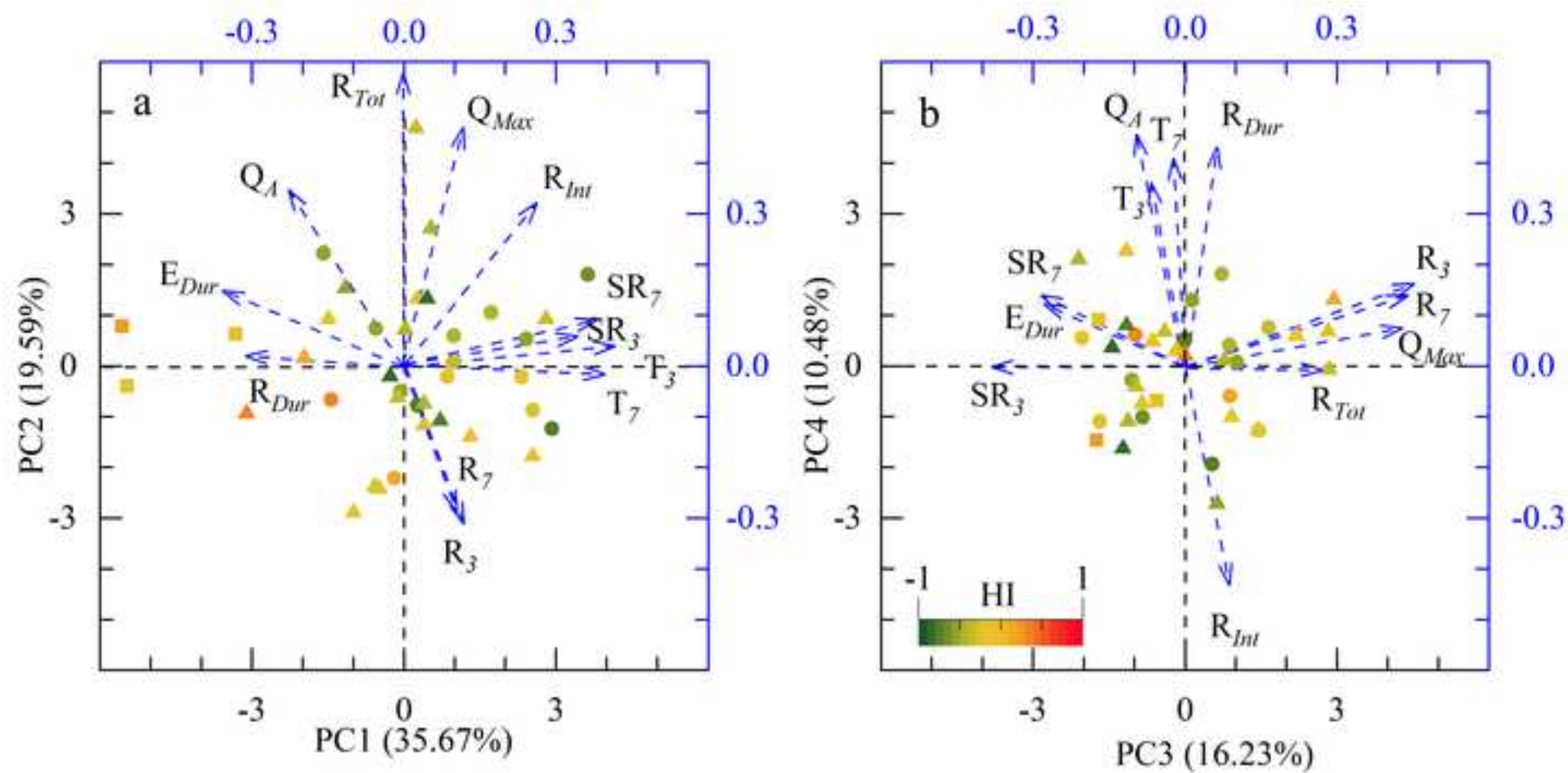


Figure 6

